TECHNICAL REPORT OF NATIONAL AEROSPACE LABORATORY

TR-447T

The Boundary Layer Separation and Shock Wave Formation due to External Disturbances in Rocket Nozzle Flow and Their Utilizations for the Thrust and Thrust-Vector Control Systems

Tetsuji NARASAKI

Mar 1978

NATIONAL AEROSPACE LABORATORY

CHŌFU, TOKYO, JAPAN

The Boundary Layer Separation and Shock Wave Formation due to External Disturbances in Rocket Nozzle Flow and Their Utilizations for the Thrust and Thrust-Vector Control Systems*

By Tetsuji NARASAKI**

ABSTRACT

When there is an external disturbace such as secondary injection or an obstacle in the supersonic nozzle flow, boundary layer separation and shock wave formation take place with various states according to the strength and position of the disturbance. Due to this boundary layer separation and shock wave formation, the pressure distribution on the nozzle-wall changes considerably, and the magnitude and direction of the thrust of the nozzle also vary with it. Therefore, these phenomena can be utilized for the thrust and thrust-vector control system of a rocket engine.

In this paper, two new systems are proposed, that is, a system for increasing the thrust of a rocket at low altitude using boundaay layer separation position control by secondary injection, and a system for thrust-vector control in which the side force is induced by a cylindrical obstacle intruding into the nozzle flow from the nozzle-wall. Theortical and experimental analyses of the related fluid dynamic phenomena were carried out, and the devices for such systems were systematically analysed and the availability of such systems was proved. The performance of these systems was confirmed by a series of firing tests of solid propellant and liquid propellant rocket engines, and enough data for the design of real rocket engines were accumulated.

When the nozzle flow is overexpanded, the boundary layer on the nozzle-wall is separated by a comparatively weak disturbance. Conversely, when the nozzle flow is underexpanded, the boundary layer is hard to separate. Even if it is separated by a rather strong disturbance, the separated boundary layer reattaches immediately thereafter and the region of the separation is very narrow; but in this case, a strong shock wave is formed in front of the obstacle, with which the pressure distribution in the nozzle changes considerably. That is, although, generally, the boundary layer separation and the shock wave formation have a relation to each other, the region of the separation is very narrow and its effect on the pressure distribution on the nozzle-wall is very small in comparison with that of the shock wave. Hereafter, the boundary layer separation due to a comparatively weak disturbance in the overexpanded nozzle flow (in which case the pressure distribution depends almost solely on the separation), and the shock wave formation due to a strong disturbance in the underexpanded nozzle flow (in which the pressure distribution depends almost solely on the shock wave) are discussed separately in this paper.

Concerning boundary layer separation and shock wave formation, a number of basic studies have been presented; however, it is defficult to analyze boundary layer separation and shock wave formation in the nozzle flow based on those basic theories, because the nozzle flow includes many complex phenomena, such as chemical reaction of exhaust gas, heat transfer to the nozzle-wall, three-dimensionality of flow field, etc. Therefore, in this paper, these problems are mainly investigated by experiments and the results are compared with the theory.

The optimum expansion ratio of a rocket nozzle is determined by the altitude of a rocket flight. Generally, a rocket engine with a larger expansion ratio produces larger thrust at high altitude, but at low altitude a region of overexpanded flow in the rocket nozzle appears in which the static pressure is lower than the ambient pressure. This pressure difference produces a reverse thrust, and decreases the total thrust of the rocket engine. Therefore, when there is a large region of overexpanded flow in the rocket nozzle, the thrust increase at low altitude is obtained by decreasing the overexpanded

---

region using the method of giving a disturbance to the flow, and this method is already known. In this paper, an improvement in the thrust increase over a wide range of altitude is proposed; that is, a system keeping the thrust at the optimum value over a wide range of altitude by displacing the separation point according to the variation of the ambient pressure is considered.

In order to evaluate the effect of this system, the thrust characteristics of rocket engines equipped with this system were numerically analysed over a wide range of altitude, using available empirical formulas. From these analytical results, the remarkable effect of this boundary layer separation position control system on thrust increase at low altitude was confirmed. The experiments on layer separation were conducted using a 300 kg thrust liquid propellant rocket engine at sea level. The secondary injection system was used for generating the separation, in which the boundary layer was forced to separate in the region of the overexpanded flow by absorbing the ambient air through holes arranged on the nozzle-wall. By this experiment, the separation characteristics of the boundary layer with or without the outer disturbance due to the injection or absorption of the ambient air through the holes were made clear, and also the thrust-increasing effect of the system at low altitude predicted analytically was confirmed.

Concerning the shock wave formation due to the strong disturbance in the underexpanded flow, the shape and the pressure distribution of the shock wave were analysed by using Taylor-Sakurai's blast wave theory, and Lee's and Zukoski's formula for the drag of the obstacle in the supersonic stream. The pressure distribution on the nozzle-wall is changed from axisymmetric to asymmetric because of the strong shock wave formation; then the side force perpendicular to the nozzle axis is induced. The values of the pressure distribution and the side force were obtained using these theories, and the relation between the side force and the shape and position of the obstacle on the hozzle-wall was given.

These analytical results were compared with the two-dimenional supersonic Wind-tunnel experiment, and it was found that the analytical results agree with the experimental results in the region close to the point of the shock wave formation. Then, the firing teste of solid propellant rocket motors of 420 kg thrust, 80 kg/cm² chamber pressure, 3.5 sec. burning duration, and a liquid propellant rocket engine of 300 kg thrust, 20 kg/cm² chamber pressure, 25 sec. burning duration, liquid oxygen and ethyl alchol were conducted, and the magnitude and the frequency responce of the side force were measured. Also, the heat resistance of the cylindrical obstacle and the height-control device of the obstacle mounted on the nozzle-wall were tested.

From these experimental and theoretical results, the usefulness of the boundary layer separation control system for increasing the thrust coefficient at low altitude and of the thrust-vector control system using the obstacle in the nozzle flow were confirmed.

概　　　要

ノズル内の超音速の流れに二次噴射または障害物などによって外乱を与えると，外乱の強さおよびその位置によって種々の状態で境界層のはく離がおこり，また衝撃波が発生する。このような境界層のはく離および衝撃波の発生によってノズル内の圧力分布は大きく変わり，その結果ノズルの推力の大きさおよび方向も変わる。したがって，この現象はロケットの推力および推力方向制御に利用できると考えられる。

この研究は，ノズル内壁からの二次噴射によってはく離位置を制御し，低高度飛行中のロケットの推力の増加を計るシステム，ノズル内壁上に円筒状の障害物を突出させて衝撃波を発生させ，推力の方向の制御を計るシステム，の二つの新らしいシステムを提案し，関連する流体力学的現象について理論的，実験的解析を行ない，それに基づくこのような装置についての詳細なシステム解析の結果，その有用性を立証したものである，また各種の固体ロケットモータ，液体ロケットエンジンの地上燃焼試験を行ない，上記システム解析の裏付を得ると共に実機の設計に対する十分な資料を与えたものである。

ノズル内の流れが過膨張の場合には比較的弱い外乱によってノズル壁面上の境界層をはく離させることができるが，過膨張でない場合には強い外乱を与えなければ境界層にはく離を発生させることはできない。また強い外乱によってはく離させたにしても境界層はその下流側で直ちに再付着し，はく

離領域は小さい。しかし，この場合には強い衝撃波が発生し，これによってノズル内の圧力分布が大きく変わる。すなわち，境界層のはく離領域は小さく，圧力分布の変動におよぼす影響は衝撃波の影響に比較して小さい。一般に，境界層のはく離および衝撃波の発生は相互関係を有するものではあるが，ノズル内の圧力分布を調べる場合には，上述のごとく，衝撃波またはく離のそれぞれの影響だけで圧力分布が定まる場合について，すなわち比較的弱い外乱により過膨張の領域に生ずる境界層のはく離の場合および強い外乱により非過膨張の領域に発生する衝撃波の場合に分けて検討することができる。

　従来，境界層のはく離および衝撃波の発生に関しては多くの基礎的研究が行なわれている。これらの理論的および実験的研究にもとずいて実際のロケットノズル内に発生する境界層のはく離および衝撃波の発生の解析を行なうことは，ロケットノズル内の流れは排気ガスの化学反応，ノズル壁えの熱伝達，流場の3次元的構造など解析を複雑にする要因が多く，これらの基礎理論に基く解析は困難であるので，本研究は主として実験によってこれらの問題を調べ理論と比較検討を行なった。

　ロケットエンジンのノズル膨張比は，ロケットの飛しょう高度によって最適値が定まり，一般に膨張比が大きいロケットノズルでは高々度において大きな推力が得られるが低高度ではノズル内の圧力が大気圧よりも低い過膨張の部分が発生し，この過膨張部と大気との圧力差はロケットの推力と逆方向の力となり推力を大きく減少させる。したがって，大きな膨張比を有するロケットエンジンの低高度における推力増加の方法として，ノズル内の流れの過膨張の領域に外乱を与え境界層をはく離させはく離領域の圧力を大気圧に近ずけることにより推力の減少を少なくする方法は周知であるが，さらに大気圧の減少に応じてノズル内のはく離位置を変えることにより低高度から高々度までの広い高度範囲にわたって推力を最適値に保持する方法を提案する。

　上述の境界層はく離位置制御の効果を評価するために，はく離位置制御を行なった場合の推力係数を近次式を用いて広い高度範囲において計算し，はく離位置制御システムは低高度において著るしい推力増加効果があることを確認した。次に推力 300 Kg の液体ロケットエンジンを用いて地上におけるはく離の実験を行なった。はく離を発生させる方法としては，過膨張ノズルのノズル壁に配置した穴から空気をノズル内に吸入することによりノズル内の流れにはく離を発生させる二次噴射の方法を用いた。これらの実験から，外乱を与えない場合のはく離状態，および大気圧をノズル壁の穴から過膨張のノズル内に吸入した場合のはく離状態を明らかにすることができ，さらに低高度における著るしいはく離位置制御の効果を確認することができた。

　一方，強い外乱によりノズル内に発生する衝撃波に関しては，Taylor および桜井等の爆風の理論，および Lee, Zukoski 等の超音速流中における障害物の抵抗に関する理論に基づいてノズル内に発生する衝撃波の形状および圧力分布を求めた。さらに強い衝撃波の発生によって，ノズルの圧力分布が軸対称性を失い，ロケットノズルに側方向の力が発生する状態に関しても解析を行ない，側分力と障害物の形状およびノズル壁面上の位置との関係式を導いた。

　この結果は二次元ノズル模型の風胴実験による衝撃波面の測定結果と比較され，衝撃波の発生点すなわち障害物の設置位置に近い範囲では良く一致することがわかった。また推力 420 Kg，燃焼圧 80 Kg/cm²，燃焼時間3.5秒，コンポジット系推進薬の固体ロケットモータおよび推力 300 Kg，燃焼圧20 Kg/cm²，燃焼時間25秒，液体酸素およびエチルアルコールの液体ロケットエンジンを用いた燃焼実験により，発生する側分力の大きさ，および周波数特性を測定し，また円柱状障害物の耐熱性およびそのノズル内における高さの制御装置の試験を行なった。

　以上述べたごとく理論計算および実験結果から，はく離位置制御システムは推力係数の増加に大きな効果があること，またノズル内の障害物による推力方向制御システムも同様にすぐれた性能を有することが確認された。

Nomenclature

A cross-sectional area of the nozzle at a particular location;

C_f nozzle thrust coefficient;

F thrust;

P pressure;

γ specific heat ratio;

Z distance from throat along nozzle axis;

n the direction perpendicular to the nozzle axis and from the point on nozzle-wall on which an obstacle is mounted to the opposite side of nozzle-wall;

U propagation velocity of shock front;

C sound velocity of undisturbed primary flow;

M mach number of undisturbed primary flow;

ρ density;

R radius of shock front; distance of shock front from the charge;

J_0, λ_1 constants from Sakurai's method ($J_0 = 0.877$, $\lambda_1 = 1.989$ at $\gamma = 1.4$ of specific heat ratio of air);

α constant of the shape of shock front surface
     $\alpha = 0$: plane
     $\alpha = 1$: cylindrical
     $\alpha = 2$: spherical;

R_0 constant of energy E ejected from charge per unit time;

E energy ejected from charge per unit time;

$g^{(i)}, h^{(i)}$ ($i = 0, 1$)   function of r/R ($0 \cdot r \cdot R$);

D drag of obstacle;

h height of obstacle;

β angle of the plane at the head of obstacle;

P_{01} stagnation pressure before the shock front near obstacle;

P_{02} stagnation pressure behind the shock front near obstacle;

C_D drag coefficient;

d diameter of cylindrical obstacle;

$\theta_n/2$ half-angle for the divergent wall;

P_l position where an obstacle is mounted;

P_A apex point of starting shock wave on the nozzle-wall;

P_r reflection point of shock wave on the oppoite side nozzle-wall;

P'_A position of P_A replaced on Z-axis, or symmetric point of P_A on the nozzle-wall;

P'_r position of P_r replaced on Z-axis or symmetric point of P_r on the nozzle-wall;

P_0 reservoir pressure of two-dimension nozzle;

F main thrust (Z-axis component);

F_s side force ($\pm n$ component);

P_c chamber pressure;

d_t throat diameter;

d_0 diameter of nozzle-exit;

l_0 distance from throat to nozzle-exit;

l distance from throat to P_l;

ε cross sectional area ratio: $\varepsilon = A_l/A_t = 4(d_l/2 + l \tan \theta_n)^2/(d_t)^2$ ($\tan \theta_n = 0.12989$);

A_l nozzle cross sectional area at the position P_l;

A_t throat cross sectional area;

C_p mean value of C_p;

C_p pressure coefficient;

$P_{(x,z)}$ pressure distribution on the nozzle-wall covered with shock wave;

$P_{x,z}$ pressure distribution on the nozzle-wall in region of undisturbed flow;

$\varDelta F_s$ integration of pressure along the circular line on the cross section of the nozzle;

$\varDelta V$ loss of volume of an obstacle in exhaust flow;

$\varDelta h$ decrease of h at the upstream side of obstacle surface after burning test;

Subscript

A ambient pressure or atmospheric pressure;

C combustion chamber or reservoir;

∞ undisturbed primary flow;

e nozzle exit;

i interaction of shock wave with boundary layer;

s separation;

t throat;

95 the position where the pressure in a region of separation rise to $0.95P_A$, (ε_{95} corresponds to ε at $p = 0.95 P_A$);

ki position of boundary layer separation forced by external disturbance (i: number);

1.INTRODUCTION

When a disturbance is introduced into a supersonic stream in a rocket nozzle generally the boundary layer separation takes place and the shock wave is formed while the pressure distribution on the nozzle-wall changes drastically.

In a case that the weak disturbance is given in a underexpanded nozzle flow the boundary layer separation hardly occurs. However when the strong disturbance by an obstacle such as a circular cylinder with a finite length attached on the nozzle-wall is given, the boundary layer separation occurs, though the region with the reverse velocity gradient is very narrow and the separated boundary layer reattaches immediately thereafter, and a strong shock wave is formed in front of the obstacle causing the large variation of the pressure distribution on the nozzle-wall. This strong shock front reaches to the opposite side nozzle-wall, reflects at the wall and rises the pressure on it. Therefore, the pressure distribution on the nozzle-wall is changed from axisymmetric to asymmet-

ric, then the side force perpendicular to the nozzle axis is induced. This side force can be used for thrust-vector control of a rocket engine.

Contrary to that, when the disturbance is given in the over-expanded nozzle flow, the separation takes place and the pressure in the region of the separated boundary layer rises strongly due to an oblique shock wave caused by shock-boundary layer interaction, and the point of reattachment moves far downstream and disappears, and the pressure in this region approaches to the ambient pressure at the nozzle exit. Therefore, when there is the large region of overexpanded flow in the rocket nozzle, some thrust increase under certain ambient pressure is obtained by decreasing the overexpanded region using this method of giving a disturbance to the flow. In this paper, the boundary layer separation due to the weak disturbance in the overexpanded nozzle flow and the shock wave formation due to the strong disturbance in the underexpanded nozzle flow are discussed separately.

Concerning the separation and the reattachment of the boundary layer, a number of basic studies have been presented (1~24). However, the analyses of the real rocket nozzle flow are very difficult, because that the nozzle flow includes many complex phenomena, such as turburent boundary layer, three-dimensionality of flow field, chemical reaction, heat transfer to the nozzle-wall etc.. In case of supersonic uniform stream along a flat plate, the distributions of the velocity, the temperature and the thickness of the boundary layer are calculated using the approximate solutions of the momentum and energy integral equations (1). The separation and the reattachment of the two-dimensional laminar boundary layer have been analysed theoretically (2~5). Especially, for the flow with a large Raynolds number, the pressure distribution in the region of the interaction of the boundary layer on a flat plate with the incident shock wave is calculated by the two-momentum method (6, 7), and its result agrees with experiments, although this method can not be applied to turbulent boundary layer in a rocket nozzle. For this case, a number of investigations based on the experiments using two-dimensional step or incident oblique shock wave have been presented (8~15). Based on the experiments of a cylindrical obstacle attached on a flat plate, Forber and Kaemper (16, 17) have given semi-empirical equation relating the angle of oblique shock wave resulting from the boundary layer separation with the flow condition and the bow-wave stand off distance with the height of the obstacle. The ratio of the upstream static pressure to the one in the separation region does not depend on the shape of an obstacle, but correlates with the reservoir pressure and the Mach number (2, 18~21). Using this relation,

the separation point can be determined. On the other hand, the reattachment point depends on the step height and the Mach number. Wanschkuhn, Roshtko, et al. conducted the experiments about the separation and reattachment of the boundary layer induced by a downstream-facing step, and measured the pressure distribution and the local shear stress (22~24).

Concerning the shock wave induced in a nozzle flow by a strong disturbance, Taylor (25) investigated theoretically the propagation of strong spherical blast wave which is caused by sudden release of a finite amount of energy at a point. Sakurai (26, 27) developed this theory and obtained the second order solution on the propagations of plane and cylindrical blast wave. Using this theory and rewriting the drag of an obstacle in supersonic stream in the form of energy, the shape of shock wave induced by an obstacle in supersonic stream is obtained. The shape of the bow shock wave caused by a forward-facing step, a blunt nosed slender body and a right circular cylinder attached on a flat plate have been investigated theoretically and experimentally (28~30), in which the drag forces are rewritten in the form of energy (28, 30).

As another method of giving a disturbance in order to separate the boundary layer, the secondary injection method is known (32~35), in which gases or liquids are injected into the nozzle flow through the holes arranged on the nozzle-wall. Thus, the pressure distribution on the nozzle-wall changes from symmetric distribution to asymmetric, and this asymmetric pressure distribution produces the side force which can be used for the thrust-vector control of a rocket engine. The drag of the secondary injection is calculated with the method of integrating the drag coefficients of the equivalent bodies by which the shock wave is induced and the shape of this shock wave is same to the one induced by the injectant penetrating into the primary stream (34). Also the method of momentum deficit of the injectant which is accelerated to the velocity of the primary stream is known as the another available method of calculating drag.

In this report, according to the abovementioned basic studies, the systems to improve the efficiency of a rocket nozzle with a large expansion ratio at sea level and to utilize the side force produced from the asymmetric pressure distribution in a nozzle are discussed. In Chapter 2, the thrust coefficients of the rocket nozzles with a large expansion ratio calculated over a wide range of altitude are compared with those of the nozzles equipped with the boundary layer separation position control system. Also, the shock wave formation due to the cylindrical obstacle in the underexpanded nozzle flow is analysed. In Chapter

3, the experiments on the boundary layer separation induced by injecting the ambient air through the holes arranged on the nozzle-wall and on the shock wave formation due to the cylindrical obstacle in the nozzle are described. In Chapter 4, the characteristics of the boundary layer separation and the shock wave formation due to the cylindrical obstacle in the underexpanded nozzle flow are discussed on the base of these experimental results. The pressure distribution and the side force are calculated and compared with the results of the experiments.

2. BASIC EQUATION

2.1 Boundary layer separation of rocket nozzle flow

2.1-(1) Thrust coefficient of the overexpanded nozzle

Generally, the optimum expansion ratio of rocket engine nozzle is larger at higher altitude but it's smaller at lower altitude. Therefore, as the ideal design of rocket nozzle, thrust can be kept on the optimum value when the expansion ratio ε varies continiously according to the altitude of rocket flight. However, in case of the practical design of a rocket nozzle, the range of the altitude is assigned previously, and ε is fixed so as to produce large total impulse in the assigned region of altitude. There is considerable difference between the thrust of a rocket engine with a constant expansion ratio and the thrust of a rocket engine with a variable expansion ratio which can take the optimum value at the arbitrary altitude, and the difference increases in proportion to the range of altitude. Therefore, the thrust coefficient of rocket nozzle with constant ε can be improved by dividing the range of rocket flight altitude into small ranges. However, if this method is used for a rocket design as it is, the rocket should be composed with a large number of stages, and the performance of the rocket will decrease extremely. Therefore, as the available method obtaining optimum thrust coefficient in the arbitrary altitude, the boundary layer separation position controlsystem is considered, and with this system a rocket of the minimum stages can be designed. The separation of the boundary layer in the range of overexpanded flow is induced by injecting the ambient air through the holes arranged on a nozzle-wall, and the separation position can be controled by shifting the injecting holes position on the nozzle-wall according to the variation of altitude. Fig. 1 shows the pressure distribution on a rocket nozzle axis. The region of the overexpanded flow extends in proportion to nozzle expansion ratio , and the difference between the pressure acting on the nozzle-wall in the region of overexpanded flow and the ambient pressure produce the reverse force which direction is reverse to

the rocket thrust. In Fig. 1, the area written with oblique line show the magnitude of the reverse force. The difference between the pressure P in the overexpanded nozzle flow and the ambient pressure P_A increases according to the increases of ε and P_A, and a boundary layer separation is induced at a certain pressure ratio P_e/P_A as shown in Fig. 2. Then, the pressure at the separation point on the nozzle-wall rise extremely, and the region of the boundary layer separation extends to the nozzle exit, and the pressure at the nozzle exit approaches to the ambient pressure.

An analytical formulation expression for the pressure rise which is required to separate the flow was provided by Aren (18), which is the function of P_A the reservoir pressure P_c and the fluid velocity U. Kalt (21) simplified this analytical formulation expression and provided the empirical equation of the pressure ratio P_i/P_A, with which the separation point can be determined directly.

Thrust F of a rocket engine is usually written as follows,

$$F = C_f \cdot P_c \cdot A_t \qquad (1)$$

where, P_c is the resorvoir or combusion pressure, A_t is the cross-sectional area at a nozzle throat. When the exhaust gas is frozen isentropic flow in a nozzle and the effect of nozzle expansion angle and the friction force acting on a nozzle-wall are negligible, C_f is given as follows,

$$C_f = \sqrt{\frac{2\gamma^2}{\gamma-1}\left(\frac{2}{\gamma+1}\right)^{(\gamma+1)/(\gamma-1)}\left[1-\left(\frac{P_e}{P_c}\right)^{(\gamma-1)/\gamma}\right]}$$
$$+ \frac{P_e - P_A}{P_c} \cdot \varepsilon \qquad (2)$$

On the other hand, thrust is calculated from the exhaut gas momentum at a throat and the pressure distribution on a nozzle-wall. The sketch of the pressure distribution is given in Fig. 3, and the equation of thrust is given as follows,

$$F = \int_{throat} P \cdot dA + \int_{throat} V\rho V dA + \int_{wall} PdA$$
$$- \int_{wall} dF_f - P_A A_e \qquad (3)$$

and C_f is given by

$$C_f = \left(\int_{throat} PdA + \int_{throat} V\rho V dA \right.$$
$$\left. + \int_{wall} PdA - \int_{wall} dF_f - P_A A_e \right) \Big/ P_c A_t \qquad (4)$$

where, V is the exhaust gas velocity, dF_f is $K_f \, q \cos\theta_w \, dA$, K_f is the coefficient of exhaust gas friction, θ_w is the half angle of divergent nozzle section, q is the exhaust gas momentum rate $\dot{m}/cm^2$. Fig. 4 shows a sketch of boundary layer separation in a nozzle, and ε_i is the nozzle area ratio at the initiation point of shock wave-turbulent boundary layer interaction, and

ε_s is the nozzle area ratio at the separation point, and ε_{95} is the nozzle area ratio where the pressure on the nozzle-wall rise to 95 percent of the ambient pressure. Dividing the region of the pressure distrubution on the nozzle-wall into three regions with the positions of ε_i and ε_{95}, the equation (3) can be rewitten as follows,

$$F=\int_{throat} PdA+\int_{throat} V\rho VdA+\int_{throat}^{\varepsilon_i} PdA$$
$$+\int_{\varepsilon_i}^{\varepsilon_{95}} PdA+\int_{\varepsilon_{95}}^{\varepsilon} PdA-\int_{throat}^{\varepsilon} dF_f-P_AA_e \quad (5)$$

In case of large ε, the friction has some effects on the thrust. However, it is not our intent to investigate the effect of the friction in this paper, and also, in case of small ε, the effect of friction is negligible (20). Therefore, the friction term in Eq. (5) is neglected in this paper, and Eq. (5) is rewitten as follows,

$$F=C_{fi}P_cA_t+\int_{\varepsilon_i}^{\varepsilon_{95}} PdA+\int_{\varepsilon_{95}}^{\varepsilon} PdA-P_AA_e \quad (6)$$

where, C_{fi} is the thrust coefficient of nozzle with expansion ratio ε_i in vacuum. Kalt and Badal (21) replaced the second term and the third term of Eq. (6) with the approximate formula as shown in the following Eq. (7),

$$F=C_{fi}P_cA_t+0.55(P_i+P_{95})(A_{95}-A_i)$$
$$-P_A(0.975A_{95}+0.025A_e) \quad (7)$$

ε_i is calculated from the following empirical equations,

$$P_i/P_A=\frac{2}{3}(P_c/P_A)^{-0.2} \quad (8.1)$$

$$1/\varepsilon_i=\left(\frac{\gamma+1}{2}\right)^{1/(\gamma-1)}\left(\frac{P_i}{P_c}\right)^{1/\gamma}\sqrt{\frac{\gamma+1}{\gamma-1}\left[1-\left(\frac{P_i}{P_c}\right)^{(\gamma-1)/\gamma}\right]} \quad (8.2)$$

and ε_{95} is calculated with the following equations,

(1)   in case of $\varepsilon_i\leqq\dfrac{\varepsilon}{1.6}+0.38$

$$\varepsilon_{95}-\varepsilon_i=(\varepsilon_i-1)/2.5 \quad (9.1)$$

(2)   in case of $\varepsilon_i\geqq\dfrac{\varepsilon}{1.6}+0.38$

$$\varepsilon_{95}-\varepsilon_i=(\varepsilon-\varepsilon_i)/1.45 \quad (9.2)$$

From the Eqs. (2), (7), (8.1), (8.2), (9.1) and (9.2), the thrust coefficients C_f can be calculated in the practical ranges of γ and ε (36), and the results are shown in Fig. 5~Fig. 9. The ranges of pressure ratio P_c/P_A, specific heat ratio γ and expansion ratio ε are given as follows, $P_c/P_A=20\sim10^4$, $\gamma=1.10\sim1.30$, $\varepsilon=3\sim200$. Fig. 10 shows the result of firing tests of 300 K_g thrust liquid propellant rocket engines at sea level. The difference between these experimental data and the calculated results C_f is less than 3 %, which is

due to the fluctuation of propellant flow and combustion pressure. Fig. 11 shows a part of the results of firing tests of 5.5 ton thrust liquid propellant rocket engine in vacuum. The data of firing tests are given in Table 1 and Table 2.

2.1-(2)   Separation position control

In Fig. 12, ε_n is the nozzle area ratio at the position of the separation which is induced naturally on the condition of ambient pressure, and ε_0 is the nozzle area ratio at the position where the static pressure P in undisturbed flow coincides with P_A, and ε_k is the nozzle area ratio at the position where the boundary layer is forced to separate by disturbance.

Giving a disturbance to a nozzle flow at the position of ε_k which is located between ε_0 and ε_n, the separation is induced and the pressure P on the nozzle-wall downstream of ε_k rises extremely, and the thrust increases as shown in Fig. 12 with the hatched area.

In Fig. 13, $\varepsilon_{ki}(i=1,2,\cdots n)$ are the nozzle area ratios at the position where separation is forced by disturbance, and ε_{ki} are slightly larger than ε_{0i}, and $\varepsilon_{0i}(i=1,2,\cdots n)$ corresponds to $P_{Ai}(i=1,2,\cdots n)$, respectively.

The conditions of this calculation are given as follows, the separation is induced at the position of the nozzle area ratio ε_k and the separation region extends to the nozzle-exit, and the nozzle area ratio ε_{95} can be calculated with Eq. (9.1) and Eq. (9.2), then, the thrust is calculated from Eq. (7).

The process of the calculation is as follows,

(1)   to calculate ε_0 from the ambient pressure

(2)   to select ε_k from $\varepsilon_{ki}(i=1,2,\cdots n)$, ε_k selected should exits most close to ε_0 downstream, and C_f is calculated with Eqs. (7), (9.1) and (9.2).

(3)   When the ambient pressure P_A varies according to the altitude of a rocket flight, process (1) and (2) are repeated.

Using the above-mentioned method, the maximum thrust at the arbitrary value of ambient pressure can be calculated by giving small values to the intervals of $\varepsilon_{ki}(i=1,2,\cdots n)$. The program of the electronic computer for this calculation is given in Appendix 1. The constants used in this calculation are as follows, $P_{ki}(i=1,2,\cdots 6)=0.597$, 0.444, 0.174, 0.070, 0.041. 0.029 kg/cm², $\gamma=1.10$, 1.20. 1.30, $P_c=20$. 40, 60, 100 kg/cm², $\varepsilon=200$.

The results of the calculation are given in Fig. 14~Fig. 17. In Fig. 18~Fig. 21, a dotted line shows the thrust coefficient C_f in the absence of the boundary layer separation position control, and a brocken line shows the envelope of the maximum value of C_f at arbitrary value of P_c/P_A.

From these results, it is ascertained that the separation position control system has an large effect on the improvement of the thrust coefficient at low altitude, especially, in case of large ε the thrust increases more than 10 percent.

2.2 The shock wave induced by an obstacle in a nozzle

2.2–(1) The shape of shock wave in a nozzle

When an obstacle is mounted on the nozzle-wall of a rocket engine near the nozzle-exit, the shock wave is induced as shown in Fig. 22 with the dashed line, and the pressure distribution on the nozzle-wall turns into an asymmetric distribution around the nozzle-axis and the side force with the direction $-n$ is induced. On the other hand, when an obstacle is mounted on the nozzle-wall near the throat, the shock front reaches to the opposite side nozzle-wall and reflects on it as shown in Fig. 22 with the solid line, and if the pressure on the opposite side nozzle-wall covered with the reflected shock wave is high enough and its area is reasonably wide, the side force with the direction n is induced.

Using the analogy of the cylindrical blast wave, the shape of shock wave and the pressure distribution which are induced by the blunt-nosed slender bodies parallel to the supersonic flow and by a right circular cylinder of finite length mounted on a wind tunnel have studied (12, 28, 29, 30), results of which have been applied to the thrust vector control by secondary injection (34, 13, 37). The similar analysis is employed for analyzing the side force induced by an obstacle mounted on the nozzle-wall.

However, concerning the side force of rocket engine, it is difficult to relate the analytical result accurately with the experimental result, because there are many unknown factors such as specific heat ratio, temperature, boundary layer, etc.. Accordingly, in order to study the characteristics of the side force induced by an obstacle mounted on the nozzle-wall, experiments with both supersonic air flow and the rocket engine firing test are necessary, and it is desirable to determine experimentally the dependence of the magnitude of side force and its direction on such parameters that characterize the size of the obstacle and the distance from the nozzle throat.

2.2–(2) Propagation and structure of blast waves

The propagation velocity and the distribution of hydrodynamic quantities of blast wave are expressed in the form of power series in $(C/U)^2$, where U is the propagation velocity of shock front and C is the sound velocity of undisturbed primary flow. Taylor found the solution (25) of the spherical blast wave for the first order approximation, and this solution corresponds to the approximation valid for the case where the ratio $(C/U)^2$ can be neglected. Then Sa-

kurai calculated the radius R (25, 27) of shock front from the charge and pressure distribution (26, 27) of blast wave with shock front surfaces of plane, cylindrical and spherical shape for the second order approximation. The radius R of the shock front and the distribution of hydrodynamic quantities are expressed as follows,

$$(C/U)^2(R_0/R)^{\alpha+1}=J_0\{1+\lambda_1(C/U)^2\}$$
$$P=P_\infty(U/C)^2\{g^{(0)}+(C/U)^2 g^{(1)}\} \qquad (10)$$
$$\rho=\rho_\infty\{h^{(0)}+(C/U)^2 h^{(1)}\}$$

where

J_0, λ_1:   constant obtained from Sakurai's method.
       $(J_0=0.877, \lambda_1=-1.989 \text{ at } \gamma=1.4)$

α: constant of the shape of shock front surface

       $\alpha=0$: plane
       $\alpha=1$: cylindrical
       $\alpha=2$: spherical

R_0:   constant of the energy E ejected from charge per unit time

$g^{(i)}, h^{(i)} (i=0, 1)$:   function of r/R, $(0 \leq r \leq R)$

$$R_0=(E/p_\infty)^{1/(\alpha+1)}. \qquad (11)$$

By mounting a two-dimensional rectangular block on the wall of two-dimensional nozzle, the oblique shock is induced, which is regarded as the plane blast wave.

In order ot analyse the shape of shock front in the supersonic flow, it is reasonable to use the coordinates fixed on the nozzle axis.

Using the relation $z/CM=t$, the propagation velocity U of shock front is expressed as follows:

$$U=dR/dt=dR/dz \cdot dz/dt=dR/dz \cdot CM \qquad (12)$$

where Z is the distance from the throat, and dz/dt is the velocity of undisturbed flow. Substituting Eq. (12) and $\alpha=0$ to Eq. (10), the following equation is obtained

$$z/(R_0 M)=$$
$$\sqrt{[J_0(-J_0\lambda_1)]^{3/2}}\{\sqrt{-J_0\lambda_1(R/R_0)}[1-J_0\lambda_1(R/R_0)]$$
$$-\log(\sqrt{1-J_0\lambda_1(R/R_0)}+\sqrt{-J_0\lambda_1(R/R_0)}\}. \qquad (13)$$

From Eq. (13), the shape of the shock front can be determined.

In case of the cylindrical obstacle, the shape of shock front is calculated in the same way also. If the obstacle of the blunt nose slender body is parallel to the nozzle-axis, the bow shock is induced from the nose of slender body. Observing this shock wave with the coordinate fixed on the undisturbed flow with the velocity dz/dt, it is regarded as the cylindrical blast wave, and Eq. (10) can be used for the analysis of the shock wave induced by a cylindrical obstacle. From Eq. (10), (12) and $\alpha=1$, the following equation is given.

$$z/R_0 M=\sqrt{J_0}\{1-\sqrt{1-J_0\lambda_1(R/R_0)^2}\}/(J_0\lambda_1). \qquad (14)$$

Concerning E and drag D of the obstacle in the flow, there are following relations

$$E=D\ (\alpha=0)$$
$$E=2D\ (\alpha=1). \tag{15}$$

and the relation between E and R_0 is given in Eq. (11).

2.2-(3) Drag of obstacle mounted on the nozzle-wall

The drag D of two-dimensional reactangular block mounted on the nozzle-wall is approximately calculated as follows,

$$D=(p_{02}-p_{\infty})h. \tag{16}$$

On the experiment with the two-dimensional nozzle, the pressure P_{∞} at the apex point P_A of the shock front is almost equal to P_{∞} at the position P_l of the obstacle on the nozzle-wall, and P_{∞} (at P_A) can be replaced by P_{∞} (at P_l), then,

$$p_{\infty}\doteqdot 0.032\ \text{kg/cm}^2\ (\text{at}\ p_l)$$
$$p_{02}/p_{01}=0.4762\ (\text{at}\ M=2.56,\ \gamma=1.4)$$
$$p_{01}=0.06\ \text{kg/cm}^2$$

Eq. (16) is

$$D=(p_{02}-p_{\infty})h=0.0254\ h. \tag{17}$$

From Eqs. (11) and (15)

$$R_0=E/p_{\infty}=0.79\ h.$$

In case of the cylindrical obstacle supported at one end on the nozzle-wall, the drag coefficient C_D was in the range of $h/d=6.42\sim 14.56$ measured by Sykes (29), from this data C_D at small values of h/d and $d=12$ mm is determined by the extrapolation as follows,

$$C_D=1.4(h/d<1,\ d=12\ \text{mm}).$$

Thus, the drag of cylindrical type obstacle can be obtained from the following equation

$$D=\tfrac{1}{2}C_D\rho u^2 hd=\tfrac{1}{2}C_D\gamma M^2 p_{\infty}hd. \tag{18}$$

From Eqs. (11), (15), (18), the constant R_0 is obtained.

3. EXPERIMENT

3.1 The boundary layer separation in an overexpanded nozzle flow

The separation in an overexpanded nozzle flow was induced with the method of injecting the ambient air through the holes arranged on the circumference which is located at the position of nozzle area ratio ε_k on the nozzle-wall. The pressure distribution on the nozzle-wall and the thrust coefficient C_f were measured for various parameters ε_k, the diameter of the hole and the number of the holes. The characteristics of the engine used are as follows:

the propellant	$LOX\text{---}C_2H_5\cdot OH$
the thrust F	300 kg
the chamber pressure P_c	20 kg/cm²

| the nozzle area ratio (exit) | 12 |
| the specrfic heat ratio γ | 1.22 |

The figures of the engine, overexpanded nozzle and test stand are shown in Fig. 23~Fig. 25, respectively. The characteristics of the nozzle used are as follows.

the type: conical, exchangeable, three types (ε_{ki} ($i=1, 2, 3$))

the area ratio (exit): 12

the area ratio at the position of holes: $\varepsilon_{ki}(i=1, 2, 3)=4.7,\ 6.0,\ 7.4$

the diameter of hole: $0\sim 9$ mm

the number of holes: 20 arranged on the circumference of the nozzle

In case of the nozzle without hole, the pressure distribution on the nozzle-wall is given in Fig. 26. The solid line shows the result of calculation on the static pressure distribution in undisturbed flow, and the dotted line shows the experimental result. The overexpanded flow exists in the region of $\varepsilon=3.5\sim 9$, and the separation occurs at $\varepsilon=9$, and the pressure rises extremely downstream of the separation point on the nozzle-wall, and approaches to the ambient pressure at the nozzle-exit.

In case of the nozzles with holes arranged on the circumference at the position of ε_{ki} ($i=1, 2, 3)=4.7$, $6.0,$ 7.4, the pressure distribution on the nozzle-wall was measured and the results are given in Fig. 27, 28, 29, respectively, and the thrust coefficients are shown in Fig. 30 with mark x and the pressure P_k which is the static pressure at ε_k.

3.2 Shock wave induced by an obstacle

3.2-(1) Observation of the shock wave in the supersonic air flow

In series of experiments with two-dimensional nozzle with 15 mm by 100 mm throat with a half-angle of $10°37'$ for divergent walls on which an obstacle is mounted at $l=78$ mm from the throat, the shape of shock wave and the pressure distribution on the nozzle-wall were measured. The dimension and characteristics of the two-dimensional nozzle are as follows:

the throat	15 mm × 100 mm
the half-angle for the divergent walls ($\theta_n/2$)	$10°37'$
the distance from throat to the position $p_l(l)$	78 mm
the diameter of cylindrical obstacle (d)	12 mmϕ
the two-dimensional obstacle (rectangular block)	$h\times 12$ mm
the obstacle height (h)	$1\sim 12$ mm
the angle of the plane at the head of obstacle to the stream (β)	$0°\sim 35°$
the reservoir pressure (p_0)	7.3 ± 0.1 kg/cm²

the Mach number of undisturb-
ed flow at p_l (M) 2.56
the distance between the posi-
tions of pressure orifices with
diameter 0.3 mm ϕ 20 mm

The photographs of the shapes of shock front and reflected shock induced by two-dimensional rectangular blocks and cylinders with various height were taken using a conventional two-mirror Schlieren system, and the pressure distribution on the wall was measured with the mercury manometer. From the observation of a series of shock fronts it can be seen that the strength of the shock wave depends on the obstacle height h. The radius R of shock front measured from the photographs is normalized and given in Fig. 33 and Fig. 34. These experimental results agrree with the analytical results calculated from Eqs. (13) and (14), where the analytical results were calculated with the hypothesis that Mach number near the obstacle is a constant value of 2.56. By rewriting the normalized R/R_0 and Z/R_0 of Fig. 33 and Fig. 34 in the form of R and z, it can be understood that the angle and the strength of shock front are roughly in proportion to the obstacle height h. The pressure distribution on the nozzle-walls with a two-dimensional rectangular block was measured by using mercury manometer of accuracy ± 1 mm Hg. The results are given in Fig. 35, which show that the pressure distribution on the opposite side wall is fairly high in comparison to the pressure distribution of the wall on which an obstacle is mounted. This high pressure distribution on the downstream from the reflection point P_r on the opposite side wall is induced by the reflected shock wave.

From the result of these experiments, it is found that the reflected shock wave generates high pressure region over the wide area on the opposite side wall, and generates the side force in the direction of n.

3.2-(2) Side force measurement with rocket engine firing test

The experiment with solid-propellant rocket engine with an obstacle mounted on the nozzle-wall was performed. The dimension and the characteristics of the rocket engine and the obstacle are as follows:

the chamber pressure (p_c)	80 kg/cm²
the thrust	420 kg
the specific impulse (I_{sp})	218 sec
the firing duration (t)	3.5 sec
the throat diameter (d_t)	20.7 mm
the diameter of nozzle-exit (d_0)	58.85 mm

the distance from throat to nozzle-exit
$\quad (l_0)$ 145.7 mm
the distance from throat to p_l
    62.6, 72.9, 82.7, 92.7, 102.7 mm
the height of cylindrical type obstacle

$\quad (h)$ 3~9 mm
the diameter of cylindrical type obstacle
$\quad (d)$ 12 mm
the material of nozzle   S25C
the cross sectional area ratio (ε)
    3.20, 3.66, 4.15, 4.68, 5.23:
the ratio of the nozzle cross sectional area A_l at the position p_l to the throat cross sectional area
A_l: $A_l/A_t = 4(d_t/2 + l \tan \theta_n)^2 (d_t)^2 (\tan \theta_n = 0.12989)$.

The thrust and the side force were measured by using "solid-propellant rocket firing stand for vertical multicomponents of thrust", by which three components of the force, a nozzle-axis component and two lateral components which are perpendicular to each other can be measured. The side force F_s which is the lateral component of the force is in proportion to the height h of obstacle except the region of the small values of F_s. Then, the direction of the side force depends on the position P_l of the obstacle. These experimental results are given in Fig. 36, from which it is found that when ε is small the side force with the direction n is induced and its magnitude is fairly large in comparison with the side force with the direction $-n$ which is induced when ε is large, and there is one particular value at which $F_s = 0$ for each value of the parameter h.

3.2-(3) Frequency response of side force

The response of side force depends on the dimension of the nozzle with an obstacle. However, it is considered that the response is very fast, and the gain in low frequency is constant and there is no phase-lag. In order to certify the frequency response of the side force, the rocket engine firing tests with the cylindrical type tungsten obstacle the height of which changes periodically were conducted.

Equipment

Fig. 37 shows the nozzle with the actuator of an obstacle, and the characteristics and dimension of the engine and nozzle are as follows:

(1) Engine

the combustion pressure (P_c)	70 kg/cm²
the main thrust (F)	370 kg
the duration (t)	4 sec.

(2) Actuator and obstacle

the electric motor 1	AC 25 W 135 rpm
the electric motor 2	AC 45W 60~500 rpm
the diameter of obstacle (d)	12 mm
the amplitude of h	0~7.1 mm
the material of obstacle	W (99%)
the frequency range	1.4~13.5 c/s
the ratio F_s/F	8%

Main features of the equipment are as follows:
(1) 0 ling is used for prevention of leakage of gas between the obstacle and the nozzle-wall.

(2) Grapthite is used on the nozzle-wall around the the obstacle to prevent melting of the nozzle-wall and to decrease the friction between the obstacle and the nozzle.

(3) The composition of propellant consists of 85% of ammonium perchlorate, 15% of polybutadiene and trace of low burning rate catalyzer. Due to the high brightness of this propellant, the photograph of the flame in short distance from the nozzle-exit can be taken

Experimental results

Fig. 38 shows the side force on the conditions $\varepsilon=3.7$, $f=1.3$ c/s. It is found that in the range of $h<4.3$ mm, the direction of F_s is negative, beyond that the direction of F_s becomes positive. The side force with the direction of n and the smaller side force with the direction of $-n$ are induced alternately.

In order to explain this phenomenon Fig. 39 is presented which is rearranged with the data of the Fig. 36. For instance, in Fig. 39, F_s is positive at $\varepsilon=4.16$, $h=9$ mm, decreases according to the decrease of h, becomes zero at $h=7$ mm, becomes negative under 7 mm of h, and when h decreases almost to zero it becomes zero again. It is seen that when $h>7$ mm and $\varepsilon=4.16$ the n component force induced on the upper part of the nozzle-wall covered with the shock wave and reflected shock wave is larger than the $-n$ component force induced on the lower part of nozzle-wall, and the side force with the direction n is generated. The flow pattern of this case is shown in Fig. 22. When $h=7$ mm the n component force induced on the upper part of nozzle-wall balances with $-n$ component force induced on the lower part of nozzle-wall, and when $h<7$ mm, the shock wave does not reach the upper part of nozzle-wall, therefore, the $-n$ component force induced on the lower part of nozzle-wall is larger than the n component force induced on the upper part of nozzle-wall. Thus, the side force with the direction n and the smaller side force with the direction $-n$ are induced alternately. It is seen that in periodic motion of the obstacle, the rate of the side force with the direction $-n$ and the side force with the direction n decreases according to the decrease of ε.

Accordingly, using small values of ε, the side force with the direction $-n$ decreases almost to zero, and frequency response of side force of 1.4~13.5 c/s of range is given in Fig. 40, which shows that the gain is constant.

3.2-(4) Heat resistance test of an obstacle

On the firing test with an obstacle of fixed height, the deformation caused by the erosion during the firing test affects variation of the side force. To maintain the control force constant the erosion of the obstacle should be minimized. The typical operating environments for the obstacle are as follows:

(1) Exposure to solid propellant combustion product

(2) 2600~3000°C of flame temperature

(3) Supersonic flame velocity

(4) Stagnation pressure load on an obstacle.

In finding refractory materials of the obstacle used in a nozzle, it is necessary to select materials with high melting point and strength. The rupture strengths in 100 hr. testing of Ni, Cr, Cb, Mo and W base alloy are given in Fig. 41 (38), which shows that the strength of Mo base alloy and W base alloy survive at high temperature, especially W base alloy has the rupture strength about 10 kg/mm² at the testing temerature 1400°C. As to the rupture strength, it is concluded that Mo base alloy and W base alloy are available for the obstacle which is used in short burning duration.

Ten refractory materials were selected for burning ing test, whose chemical composition and the melting points are given in Table 3. A series of experiments with the obstacles of refractory material were conducted with the solid-propellant rocket motor, whose performance and dimension are already described in Section 3.2-(2). The dimension of the obstacle is given in Fig. 42-(1) and -(2). In Fig. 42-(2), h is the initial height of obstacle in the nozzle. Fig. 42-(3) shows the shape measured after burning test, α is the angle of the plane at the head of obstacle, and Δh is the decrease of h. Experimental results are given in Table 4. Table 4 shows that $CM-554$ and W are fairly good characteristics for the loss of obstacle volume ΔV in the exhaust flow, and Fig. 43 shows the variation of the side force in burning duration.

It is assumed that the magnitude of the side force depends on the shape of head of obstacle and the maximum value is induced at an instant when the shape of obstacle is eroded to a cirtain shape. The time when the obstacle deforms to this shape is determined from the time when the maximum value of the side force apears. It is considered that if the peak point of the side force is near left side in Fig. 43, the rate of erosion in unit time or damage of obstacle is large and vice versa. Thus, from Fig. 43 it is inferred that the rate of erosion of $S-816$ C is faster than $CM-554$.

Thus, it is found that tungsten and $CM-554$ are advantageous as obstacle although tungsten is low in its strength (39, 40). Concerning $CM-554$, the rupture strength at high temperature is comparably low in value, as shown in Fig. 41, but C_r has highest melting point 1875°C among the metals with the antioxide performance, therefore $CM-554$ can be used for the material of obstacle in short burning duration.

In addition, for the heat resistance test of an obstacle in the long duration, firing tests were conducted

with 300 kg thrust liquid propellant rocket engine. The obstacle is a rod of cylindrical type, made of stainless steel, and cooled with water circulating inside the rod, and the height of the rod is controled with a hydraulic actuator and a servo valve. Fig. 44–(1) and –(2) show the engine and the rod height control system respectively.

The results of burning tests show a excellent performance for the heat resistance. That is, after about 300 seconds of total duration of the burning test, any deformation or damage of the rods were not found.

4. DISCUSSION

As shown in Fig. 27, 28, 29, the pressure in the separation region increases gradually according to the increase of the area of holes, and boundary layer separation occurs scarcely near the throat. According as the injection points approach to the nozzle-exit, the separation occurs easily and the separation region enlarges and extends to the nozzle-exit as shown in Fig. 28 and Fig. 29.

The experimental data C_f shown in Fig. 30 with mark x approach to the result of the numerical calculation shown with solid line according the increase of sum of the cross sectional areas of holes, and also, in case of the nozzle with the injection holes near the throat where P_k approaches to P_A, there is much difference between the experimental data C_f and the result of the numerical calculation. It is found that the above mentioned characteristics of the separation depend on the magnitude of disturbance which is in proportion to the diameter of hole, on the pressure ratio P_k/P_A and on the reattachment of the separated boundary layer.

In the numerical calculation on the thrust coefficient of a nozzle with a separation position control system, the following assumption are used, a number of holes are arranged on the circumference of the nozzle at the position of ε_k, and the separation is induced uniformly from the circumference. On the other hand, as shown in the experiment of a secondary injection and the experiment of a cylindrical obstacle supported at one end on the nozzle-wall, the separation of the boundary layer starts around the holes or the cylindrical obstacle and extends downstream. These traces of the separation are marked on the nozzle-wall clearly after a cirtain kind of firing test. In case of one hole or one obstacle set on the nozzle-wall, the trace marks a parabolic shape. When the distance of the holes arranged on the circumference are larger than the diameter of the holes, the trace will marks a sine wave with a large amplitude, and the average separation position which is obtained from the trace shifts

slightly downstream of the hole position. In case of the short distance of the holes, the displacement of the average separation position is small. Using this average separation position, the result of numerical calculation of C_f will decrease slightly.

In this experiment, twenty holes were arranged on the circumference of the nozzle, and the displacement of the average separation position was ascertained by the measurements of the pressure distribution and the traces of the separation. From these results, it can be considered that in case of $d > 4.0$ mm, $n = 20$ and $\varepsilon_k = 7.4$ the displacement is less than 10 mm, and pressure variation of P_k is about $\Delta P_k < 0.02$ kg/cm^2.

The shape of the shock front induced in a nozzle can be calculated from Chapter 2, and in this paper, the shape of the shock front and the pressure distribution in a nozzle flow are calculated under the following conditions of flow field; Mach number of the free stream is constant and the direction of the free stream is parallel to the nozzle axis. Therefore, there is some difference between the result of calculation and the experimental data at the point of a distance from the obstacle.

In order to compare the experimental results with theoretical analysis, the specific heat ratio γ, the Mach number and the pressure distribution P_∞ of free stream in the nozzle, the chamber pressure P_c and R_0 should be given. The pressure distribution P_∞ for $\gamma = 1.10$, 1.25 and 1.40, were calculate by employing the value of $P_c = 80$ kg/cm^2 which is obtained from the experimental results of the rocket engine firing test. The analytical result of P_∞ at $\gamma = 1.25$ is agrees well with the experimental result of the rocket engine firing test. Thus, using 1.25 as the value of the specific heat ratio γ, J_0 and λ_1 in Eq. (10) are determined as $J_0 = 1.29$, $\lambda_1 = -2.30$ by the Sakurai's method (26, 27).

Concerning constant R_0, the relations between R_0, the energy per unit length and time, and the drag force are given in Eqs. (11), (15) and (18). Zukoski (41) expressed the drag of the blunt nose cylindrical body with the axis parallel to the flow. Developing this method, the drag of the plate with the leading edge of half cylindrical surface can be calculated. By using the relation $C_p/C_p{}^* = \sin^2 \alpha \cdot \alpha / \sin \alpha^*$ and $C_p{}^* = (P_{02} - P_\infty)/(1/2 \cdot \rho_\infty V^2{}_\infty)$, pressure coefficient C_p can be eliminated, where α is the angle between the local tangent to the surface and the undisturbed flow direction and must lie between 0 and $\pi/2$. Here, $C_p{}^*$ and α^* are evaluated at the nose of the body. Hence, $\alpha^* = \pi/2$, and $C_p{}^*$ is the pressure coefficient corresponding to the stagnation pressure behind a normal shock and is a function of the free stream Mach number and specific heat ratio. The integral of the drag coefficient of the plate is expressed as follows,

$$\int C_D ds = \bar{C}phd = \int_0^{d/2} hCp^* \sin^2 \alpha\, dr = \tfrac{2}{3}Cp^*hd.$$

Thus, the drag is

$$D = \tfrac{1}{2}\gamma M^2 P_\infty \bar{C}_D hd = \tfrac{1}{3}\gamma M^2 P_\infty Cp^* hd. \qquad (19)$$

Using the drag of this plate instead of the cylindrical obstacle, R_0 is determined, and the radius R of the shock wave is calculated from Eq. (14).

Concerning the pressure distribution, $g^{(0)}$ and $g^{(1)}$ in Eq. (10) are the function of r/R ($0 \leq r \leq R$), and $(C/U)^2$ is the function of R only and P_∞ is the function of z. Therefore, it is considered that the pressure distribution is determined by the shape of the shock front. By integrating n component of the pressure $P(x, z)$ and $P_s(z)$ on the nozzle-wall, the side force F_s can be calculated, where $P(x, z)$ and $P_s(z)$ are shown in Fig. 45.

$$F_s = \int_{P_A}^{P_r} \left\{ \int_{-\theta_0}^{\theta_0} P(x, z) \cos\theta\, r_n(z)d\theta \right.$$
$$\left. + \int_{\theta_0}^{2\pi-\theta_0} P_s(z) \cos\theta\, r_n(z)d\theta \right\} dz + C \qquad (20)$$

where

$$r = \sqrt{(r^2_n + r^2_0 - 2r_n r_0 \cos)}$$
$$r_n(z) = d_t/2 + z \tan(\theta_n/2)$$
$$x = r/R$$

C: compensation term which depends on the reflected shock wave, in the region $p_r < z < l$.

In case when ε is large and the shock wave does not reflect on the opposite side wall, C is negligibly small. In this calculation, there is an assumption that the apex point p_A of the shock front coincides with the obstacle position p_l. In the experimental result, it is found that p_A is e mm upstream side to p_l. Therefore, the analytical result obtained from Eq. (20) lies a little toward the right side on the coordinate axis in comparison with the experimental result as shown in Fig. 36. The analytical results which are compensated with e are given in Fig. 46

By the use of proper nozzle material and propellant for firing test of rocket engine, the trace of shock front survives on the nozzle-wall as shown in Fig. 47. The trace is caused by the discontinuity of temperature distribution before and behind the shock wave, and the trace is generated along the cross-line by two surface of the shock front and the nozzle-wall. The radius R calculated by measuring the trace is given in Fig. 48, from which it is found that when ε is small the reflecting position P_r of the shock front on the opposite side wall is near the throat and it agrees with the analytical result with good accuracy.

The pressures at a few points on the nozzle-wall were measured with the strain gauge type pressure pickups, and the results are given in Fig. 49 which shows that the pressure downstream of the reflection

point P_r of the shock wave is fairly large. The pressure distribution along the circular line on the cross section of the nozzle-wall and its integrated values ΔF_s are calculated by Eq. (10) and (20), and shown in Fig. 50. From these results it is obvious that as the shock front approaches to the opposite side wall, the pressure on the ooposite side wall increases, and the direction of ΔF_s changes from $-n$ to n.

Thus, the causes of the generation of the side force with the direction n are considered as follows. (1) in a part of the area covered with the reflected shock wave on the opposite side wall, the pressure increases radically, (2) when the shock wave reflects on the opposite side wall, the direction of ΔF_s near P_r becomes n and the integration of ΔF_s along z-axis from P'_A to P'_r becomes small magnitude of the force with the direction $-n$.

Then, the side force with the direction $-n$ is generated under the following condition, the position of the obstacle is near the nozzle-exit and the shock front does not approach to the opposite side wall.

As shown in Fig. 36, the side force ratio to the main thrust can be obtained easily more than 10% when the shock wave reflects on the opposite wall, and more than 5% when the shock wave doesn't reach to the opposite wall. The frequency response of the side force shows good characteristics also. These performances of the side force induced by an obstacle are comparable with the performance of *LITVC* (Liquid Injection Thrust Vector Control) (35, 42). Especially, this system does'nt need injectant, and the reduction of fuel weight can be expected. Therefore, this system is considered as an available system for thrust-vector control system.

5. CONCLUSION

The boundary layer separation and the shock wave induced by a distrubance in a supersonic nozzle flow were studied, and the posibility of their utilization to the optimum thrust control system and the thrust-vector control system were analysed. Thrust coefficients of rocket nozzle with large expansion ratio were calculated in a wide range of altitude. In order to keep the thrust coefficient at the optimum value over a wide range of altitude, a boundary layer separation position control system was proposed, and the thrust coefficients of such system are presented systematically. The experiments on the forced separation of the boundary layer in the overexpanded nozzle flow were conducted with 300 kg thrust liquid propellant rocket engine at sea level. The results of these analytical and experimental studies are as follows.

(1) In the absence of a boundary layer separation

control system, the thrust coefficients are calculated and presented to be used for estimation in the range of $\varepsilon=3\sim200$, $\gamma=1.10\sim1.30$, and in a wide rage of altitude.

(2) The relations between the diameter and the position of the holes arranged along a circumference of the nozzle and the pressure ratio P_i/P_c and the pressure distribution on a nozzle-wall were found.

(3) The result of calculation shows a separation position control system for a rocket nozzle with a large expansion ratio increases the thrust coefficient about 10% in low altitude. Firing tests of this system were conducted and about 3~6% increase of the thrust coefficient was obtained at sea level.

Therefore, the effect of the separation position control on the improvement of thrust coefficient is remarkable, and a rocket engine with this system can be used effectively over a wide range of altitude.

Concerning the shock wave induced in a nozzle flow by strong disturbance ,a series of two-dimensional supersonic wind-tunnel experiments and rocket engine firing tests were conductd, and the pressure distribution on the nozzle-wall and the shape of shock wave induced by an obstacle were measured. These experiments were conducted under the following conditions.

Wind tunnel experiment:

(1) two-dimensional supersonic nozzle with an obstacle of rectangular or cylindrical block

(2) Mach number of the undisturbed flow at the obstacle position; 2.56

(3) half-angle for the divergent wall $\theta_n/2$; $10°37'$

(4) throat area; 15×100 mm

Rocket engine firing test (solid propellant)

(1) chamber pressure P_c; 70~80 kg/cm²

(2) throat diameter d_t; 20.7 mm

(3) nozzle expansion angle θ_n; 15°

(4) distance from throat to nozzle-exit; 145.7 mm

(5) obstacle height h; 0~9 mm

(6) obstacle diameter; 12 mm

(7) firing duration; 3.5 sec.

(8) component of propellant; 85% of ammonium perchlorate, 15% of polybutadiene, trace of low burning rate catalyzer

Frequency responce of side force

(1) amplitude of h; 7 mm

(2) frequency range; 1.4~13.5 Hz

Rocket engine firing test (liquid propellant)

(1) propellant; $LOX-C_2H_5\cdot OH$

(2) chamber pressure P_c; 20 kg/cm²

(3) throat diameter d_t; 37 mm

(4) cooling of rod; water circulating inside the rod

(5) firing duration; 25 sec.

From these experiments the characteristics of the side force induced by an obstacle mounted on the

nozzle-wall is found as follow:

(1) The magnitude and the direction of the side force are determined as a function of the height of obstacle in the nozzle and the distance of obstacle from throat.

(2) When an obstacle is near the throat the shock wave reflects on the opposite side nozzle-wall, and large side force with the direction from the obstacle to the opposite side nozzle-wall is induced.

(3) The frequency response of the side force is constant over 1.4~13.5 Hz

(4) The rod cooled by water circulation showed the excellent performance of heat resistance in about 300 sec. burning test.

From these resluts, it is considered that this thrust-vector control system is more useful than Liquid Injection Thrust-Vector Control System (35, 42).

ACKNOWLEDGEMENTS

REFERENCES

1   D. R. Bartz; An Approximate Solution of Compressible Turbulent Boudary-Layer Development and Convective Heat Transfer in Convergent-Divergent Nozzle, Transaction of The ASME, 1235–1245, (November 1955) Paper No. 54–A–153

2)   G. E. Gadd; Interactions Between Wholly Laminas or Wholly Turbulent Boundary Layers and Shock Wave Strong Enough to Cause Separation, J. Aer. Sci., Vol. 20, No. 11 (1953)

3)   D. R. Chapman, D. M. Kuehe, and H. K. Larson; Investigation of Separated Flows in Supersonic and Subsonic Streams with Emphasis on The Effect of Transition, NACA Report 1356 (3869), (March 1957)

4)   K. Stewartson and P. G. Williams; On Self-Induced Separation II, Mathematika Vol. 20, (June 1973) pp98-108

5)   Peter Thiede und Franz Otte; Theoretische Untersuchungen zur Laminarhaltung der Kompressiben Grenzschicht durch Schlitzabsangung, Zeitschrift fur Flugwissenschaften 23 Jahrgang, Heft 1 (1975) 9-24

6)   Philip M. Gerhart; On Prediction of Separated Layers with Pressure Distribution Specified

7)   Keiichi Karashima; Separated and Reattaching Flow in Supersonic Stream, Journal of The Japan Society for Aeronautical and Space Sciences, Vol. 24, No. 265, (1976)

8) W. C. Rose, J. D. Murphy and E. C. Watson; Interaction of an Oblique Shock Wave with a Turbulent Boundary Layer, J. AIAA, Vol. 6, No. 9 (Sep. 1968) pp 1792-1793

9) Kurt Nixdortt; Zur Numerischen Bestimmung der Grenzschicht hinter einer Strosswelle, Forschung im Ingeniear Wessen, Vol. 39, No. 5, (1973)

10) E. E. Zukoski; Turbulent Boundary-Layer Separation in Front of a Forward-Facing Step, J. AIAA. Vol. 5, No. 10, (Oct, 1967) pp 1746-1752

11) Robert W. Halprin; Step Induced Boundary-Layer Separation Phenomena, J. AIAA, Vol. 3, NO. 2, (Feb. 1965) pp 357-359

12) J. C. West Kaemper; Step-Induced Boundary-Layer Separation Phenomena, J. AIAA, Vol. 4, NO. 6, (June 1966) pp 1147-1148

13) Richard T. Driftmyer; Thick, Two-Dimensional, Turbulent Boundary Layers Separated by Steps and Slot Jets, J. AIAA, Vol. 12, No. 1, (January 1974) pp 21-27

14) C. Herbert Law; Supersonic Turblent Boundary-Layer Separation; J. AIAA, Vol. 12, NO. 6, (June 1974) pp 794-797

15) Michael S. Holden; Experimental Studies of Separated Flows at Hypersonic Speed Part II: Tow-Dimensional Wedge Separated Flow Studies, J. AIAA, Vol. 4, No. 5, pp790-799

16) C. Forber Dewey Jr.; Near Wake of a Blunt Body at Hypersonic Speeds, J. AIAA, Vol. 3, NO. 6, (June 1965) pp1001—,

17) J. C. West Kaemper; Turbulent Boundary-Layer Separation Ahead of Cylinders, J. AIAA, Vol. 6, No. 7, (July 1968) pp 1352-1355

18) M. Arens and E. Spiegler; Shock-Induced Boundary Layer Separation in Overexpanded Exhaust Nozzle, J. AIAA, Vol. 1, No. 3, (1963)

19) S. M. Bogdonoff and C. E. Kepler; Separation of a Supersonic Turbulent Boundary-Layer, Journal of The Aeronautical Sciences, (June 1955)

20) J. H. Ahlberg, S. Hamilton, D. Migdal, and E. N. Nilson; Truncated Perfect Nozzles in Optimum Nozzle Design, ARS Journal, (May 1961) pp 614-620

21) Sherwin Kalt and David L. Badal; Conical Rocket Nozzle Performance under Flow-Separated Conditions, J. Space Craft, Vol. 2, No. 3, (May-June 1965) pp 447-449

22) Peter Wausch Kuhn und Venkatesa I. Vasanta Ram; Die turbulente Grenzschicht hinter einem Ablosungsgebiet, Zeitschrift fur Flugwissenschaften 23 Jahrgant, Heft 1, (1975) 1-8

23 P. Wanschkuhn und V. Vasanta Ram; Die turbulente Grenzschicht unmittelbar hinter dem Wiederanlegen eines Ablosungsgebietes, Zeitschrift fur ange wante Mathematik und Mechanik, Vol. 55, (Apr. 1975) 166-168

24) A. Roshtko and G. J. Thomke; Observations of Turbulent Reattachment behind an Axisymmetric Downstream-Facing Step in Supersonic Flow, J. AIAA, Vol. 4, No. 6, (June 1966) pp975-980

25) G. I. Taylor; The Formation of a Blast Wave by a very Intense Explosion I. Theoretical Discussion, Proc. Roy. Soc., Vol. 201. A, (March 1950) pp159-174

26) Akira Sakurai; On The Propagation and Structure of The Blast Wave I, J. The Physical Society of Japan, Vol. 8, No. 5, (1953) pp662-669

27) Akira Sakurai; On The Propagation and Structure of The Blast Wave II, J. The Physical Society of Japan, Vol. 9, No. 2, (1954)pp256-266

28) L. Lees and T. Kubota; Inviscid Hypersonic Flow Over Blunt-Nosed Slender Bodies, J. Aeronautical Sci., (March 1957) pp195-202

29) D. M. Sykes; The Supersonic and Low-Speed Flows Past Circular Cylinders of Finite Length Supported at One End, J. Fluid Mech., (Dec. 1961) pp367-387

30) Thomas Daniel Butler; Numerical calculation of The Transient Loading of Blunt Obstacles by Shocks in Air, J. AIAA, Vol. 4, No. 3, (1966) pp460-467

31) H. Tao-Sze Hsia, H. S. Seifert and K. Karamcheti; Shockes Induced by Secondary Fluid Injection, J. Spacecraft, Vol. 2, No. 1, (1965) pp67-72

32) R. D. Guhse and H. Doyle Thompson; Some Aspects of Gaseous Secondary Injection with Apprication to Thrust Vector Control, AIAA Paper No. 71-750

33) A. B. Billet; Rocket Engine Thrust Vector Control Operation Through Secondary Injection, SAE Paper 865E

34) James E. Broadwell; Analysis of The Fluid Mechanics of Secondary Injection for Thrust Vector Control, J. AIAA, Vol. 1, No. 5, (1963)

35) Ryojiro Akiba; A simple Theory of LITVC, Journal of The Japan Society for Aeronautical and space Sciences, Vol. 22, No. 247, (Aug. 1974)

36) T. Narasaki, S. Ogiwara, S. Yoshihara; The Graphes of Liquid Rocket Propellant Performances, Technical Memorandum of National Aerospace Laboratory, TM-295 (1975)

37) Krishnamurty Karamcheti and Herry Tao-Sze Hsia; Integral Approach to an Approximate Analysis of Thrust Vector Contral by Secondary Injection, J. AIAA, Vol. 1, No. 11, (1963)

38) R. Yoda; Superalloys and Refractory Metals, Manufacture and Product, Tokyo, No. 8, pp45-58, (Written in Japanese) (1963)

39) G. A. Etemad; Oxidation and Mechanical Performance of Tungsten at High Temperatures and High Pressures, J. AIAA, Vol. 4, No. 9, (Sep. 1966) pp 1543-1548

40) J. E. White; Development of Oxidation Resistant Tungsten-Base Alloys, J. AIAA, Vol. 4, No. 2, (Feb. 1966) pp307–312

41) Zukoski, Edward E. and Spaid, Frank W.; Secondary Injection of Gases into a Supersonic Flow, J. AIAA, Vol. 2, No. 10, (1964) pp1689–1696

42) Daikichiro Mori; Project of M-3C, Journal of The Japan Society for Aeronautical and Space Sciences, Vol. 23, No. 257, (1975)

APPENDIX 1   PROGRAM LIST 1

SYMBOLS

EE: ε
PC: P
AK: γ
AT: A_t
PA: P_A
PS(K): P_{ki}
ES: ε_s
E95: ε_{95}
PR: P_c/P_A
F: F

1. CONICAL ROCKET NOZZLE PERFORMANCE UNDER FLOW SEPARATION CONTROL
   (thrust coefficient)

FACOM 230-75 M7   FORTRAN-IV H COMPILER (OPTO) SOUCE PROGRAM LIST

```
ST-NO                 SOUCE PROGRAM
C       FLOW-2
C       CONICAL ROCKET NOZZLE PERFORMANCE UNDER FLOW SPARATION CONTROL
C       EE, PC, AK, AT, PA, PS, ES, E95, PR, F
        DIMENSION EE(50), PS(50), PA(50), AK(50), PC(50)
        READ (5, 101) KM, JM, MM, IM, LM, AT
    101 FORMAT (5I10, F12.5)
        READ (5, 120) (PS(K), K=1, KM)
    120 FORMAT (6F12.5)
        READ (5, 130) (PA(J), J=1, JM)
    130 FORMAT (6F12.5)
        READ (5, 140) (PC(M), M=1, MM)
    140 FORMAT (6F12.5)
        ERAD (5, 150) (EE(I), I=1, IM)
    150 FORMAT (6F12.5)
        READ (5, 160) (AK(L), L=1, LM)
    160 FORMAT (6F12.5)
        DO 100 M=1, MM
        DO 90 L=1, LM
        DO 80 I=1, IM
        WRITE (6, 105) I, PC(M), EE(I), AK(L)
    105 FORMAT (1H1/10X, 2HI=,I2, 5X, 3HPC=, F5.1, 5X, 3HEE=, F5.1, 5X, 3HAK=, F5.2)
        WRITE (6, 103)
    103 FORMAT (1H0, 5X, 1HF, 6X, 2HCF, 7X, 5HPC/PA, 5X, 5HPA(J), 5X, 5HPS(K), 5X, 2HES,
       1 5X, 3HE95, 5X, 1HK, 4X, 1HJ/)
        DO 70 K=1, KM
        DO 50 J=1, JM
        E1=((AK(L)+1.0)/2.0)**(1.0/(AK(L)-1.0))*(PS(K)/PC(M))**(1.0/AK(L))
        E2=((AK(L)+1.0)/(AK(L)-1.0))*(1.0-((PS(K)/PC(M))**((AK(L)-1.0)/AK(L))))
        E3=SQRT(E2)
        E4=E1*E3
        ES=1.0/E4
```

```
            EEE=EE(I)-0.1*EE(I)
            IF(ES.GT.EEE) GO TO 80
            IF(PS(K).GT.PA(J)) GO TO 70
            E95=ES+0.1*ES
            AS=AT*ES
            AE=AT*EE(I)
            A95=AT*E95
            B1=2.0*AK(L)**2.0/(AK(L)-1.0)*(2.0/(AK(L)+1.0))**((AK(L)+1.0)/(AK(L)-1.0)
            B2=1.0-(PS(K)/PC(M))**((AK(L)-1.0)/AK(L))
            B3=PS(K)/PC(M)*ES
            CFS=SQRT(B1*B2)+B3
            F1=PC(M)*AT*CFS
            F2=0.55*(PS(K)+0.90*PA(J))*(A95-AS)
            F3=(0.975*A95+0.025*AE)*PA(J)
            F=F1+F2-F3
            CF=F/(AT*PC(M))
            PR=PC(M)/PA(J)
            WRITE (6, 110) F, CF, PR, PA(J), PS(K), ES, E95, K, J
        110 FORMAT (1H , F8.1, F8.3, F10.1, 2F10.3, 2F8.2, 2I5)
         50 CONTINUE
         70 CONTINUE
         80 CONTINUE
         90 CONTINUE
        100 CONTINUE
            STOP
            END
```

APPENDIX 2   PROGRAM LIST 2

SYMBOLS

AL:	λ constant
AJO:	J_0 constant
A:	α nozzle half angle
GX:	$g^{(0)}$ function of r/R
PX:	ψ variable
PX2:	φ variable
G1:	subroutine for $g^{(0)}$, ψ, φ
DAI:	throat diameter
Y:	nozzle radius at the position of an obstacle (r_0)
D:	drag of an obstacle
HIGHT:	hight of an obstacle
PRO:	free stream pressure at the position of an obstacle (P_∞)
AN:	mach number at the position of an obstacle
AM:	mach number
ZI:	distance form throat to an obstacle
Z:	distance from an obstacle
RI:	nozzle radiuos (r_n)
R:	radious of shock wave
POI:	combutsion pressure
G:	specific heat ratio (γ)
RO:	$(E/2\pi P_\infty)^{1/2}$
DX:	interval of computation
DZ:	interval of integral
THE:	angle of shock wave (θ_0)
PPS:	pressure on the nozzle wall

PFP: pressure distribution of inside of shock front
SI: side force on area of $2\pi R_1 \cdot DZ$
SF: total side force

2.1   SIDE FORCE

Drag
Shock wave
Pressure distribution
Side force

```
        HARP 5020 COMPILED LIST
           EXTERNAL FORMULA NUMBER—SOURCE STATEMENT
C     SIDE FORCE
      COMMON Y, PRO, AL, D, R2, AJO, AN, DX
      COMMON /C2/Z, R1, R
      COMMON /C3/A, G
      COMMON /C4/RO, DZ
      COMMON /C5/PO1
      COMMON GX(201), PX(2, 201), PX2(2, 201)
      DIMENSION S1(201), PPS(101), PFP(101, 11), THEATA(101, 11)
      DIMENSION THEAT (200), PFP1(200)
      READ (5, 1) G, AJO, AL, DAI, DEX, DB, DZ
    1 FORMAT (7F10.3)
      A=1.0
      DX=-0.01
      RSTAR=DAI/2.0
      RAED(5, 9) ZO, Z1, PO1, BOLTH
    9 FORMAT (4F10.3)
      TAN1=(DEX-DAI)/2.0/ZO
      HIGHT=BOLTH-DB/2.0*TAN1
  100 CONTINUE
      Z=0.0
      Y=RSTAR+TAN1*Z1
      E1=((RSTAR+TAN1*Z1)/RSTAR)**2
      CALL SMACH(AN, G, E1)
      PRO=PS(0.0)
      AM=AN
      D=G*PRO*AM**2*HIGHT*12.0/2.0
      PO2=PO1*(1.0+2.0*G/(G+1.0)*(AM**2-1.0))**(1.0/(1.0-G))
    1   *((G+1.0)*AM**2/((G-1.0)*AM**2+2.0))**(G/(G-1.0))
      CD=4.0/3.0*(PO2-PRO)/G/PRO/AM**2
      D=CD*D
      CP=3.0/2.0*CD
      WRITE(6, 2)G, AJO, AL, DAI, ZO, TAN1, PO1, Z1, D, DZ, E1, CP, CD, HIGHT
    2 FORMAT(1H1, 9X1H=, F6.3/8X3HJO=, F6.3/10X, 1H=, F6.3/8X3HD*=, F6.3/
    1   8X3HLO=, F7.3/6X5HTAN =, F11.8/8X3HPO=, F6.3/9X2HL=, F6.3/9X2HD=,
    2   F7.3/8X, 3HDZ=, F6.3/9X2HE=, F6.3/8X3HCP=, F7.4, 5H (CD=, F7.4, 2H )
    3   /9X2HH=, F6.3
    4   ////4X1HZ, 8X1HM, 11X1HR, 20X2HP1, 10X2HP2, 10X2HP2, 9X2HR1, 7X2HN1,
    5   6X2HN3, 7X1HF)
      D=2.0*D
      RO=DSQRT(D/2.0/3.1416/PRO)
      EXTERNAL FP
      EXTERNAL PS
      D1=D
      CALL G1
```

```
     D=D1
     N2=IFIX((ZO+0.001-Z1)/DZ)+1
     DO 10 I=1, N2
     R1=RSTAR+TAN1*(Z1+Z)
     AA=(R1/RSTAR)**2
     CALL SMACH (AN, G, AA)
     R=(2.0*D/3.1416/AJO/PRO)**0.25*(Z/AM)**0.5*(1.0-AL*(3.1416*AJO*
   1    PRO/2.0/D)**0.5/AM*Z)**0.5
     IF(R-Y-R1) 40, 50, 50
  40 S=(Y+R1+R)/2.0+0.0001
     THE=2.0*DATAN((((S-R1)*(S-Y)/S/(S-R))**0.5)
     GO TO 60
  50 THE=3.1416
     WRITE (6, 6)
   6 FORMAT (1H ,)
  60 CONTINUE
     N1=IFIX(THE/DZ*R1)+1
     N3=IFIX((3.1416-THE)/DZ*R1)+1
     DO 20 J=1, 11
     TH=THE*FLOAT(J-1)/10.0
     THEATA(I, J)=TH*57.296
  20 PFP(I, J)=FP(TH)/COS(TH)
     IF(I.NE.30) GO TO 25
     DO 22 J=1, N1
     TH=THE*FLOAT(J-1)/FLOAT(N1-1)
     THEAT(J)=TH*57.296
     PFP1(J)=FP(TH)/COS(TH)*100.0
  22 CONTINUE
     N1N=N1
  25 CONTINUE
     PPS(I)=PS(0.0)
     THF=THE*57.296
     S1(I)=2.0*(
   1    SEKBN1(FP, 0.0, THE, N1)+SEKBN1(PS, THE, 3.1416, N3))*R1
     WRITE (6, 3) Z, AN, R, THF, PPS(I), PFP(I, 1), PFP(I, 11), R1, N1, N3, S1(I)
   3 FORMAT (1H   , F5.1, F11.4, F11.3, F10.3, 3F12.5, F11.3,2I7, F12.5)
     IF(THE.LE.0.0) GO TO 30
  10 Z=Z+DZ
  30 SF=SEKBN3(S1, DZ, N2)
     WRITE (6, 4) SF
   4 FORMAT (1HO, 12HSIDE FORCE=, F8.4, 3H KG/1H1, 21HPRESSURE DISTRIBUTION)
     Z=0.0
     DO 70 I=1, N2, 5
     WRITE (6, 5) Z, PPS(I), (THEATA(I, J), J=1, 11), (PFP(I, J), J=1, 11)
   5 FORMAT (1HO, 3H Z=, F6.2, 10X, 3HPS=, F8.5/1H , 3HTH=, 11F10.3/1H , 3H P=,
   1    11F10.5/)
  70 Z=Z+DZ*5.0
     WRITE (6, 7) PPS(30)
   7 FORMAT (1H1, 3HPS=, F8.5/1H , 5(5X, 2HTH, 8X, 1HP, 8X))
     WRITE (6, 8) (THEAT(I), PFP1(I), I=1, N1N)
   8 FORMAT (1H , 5(2F10.3, 4X))
     Z1=Z1+2.5
     IF(Z1.LT.ZO) GO TO 100
     STOP
     END
```

```
      FUNCTION FP(TH)
      COMMON /C2/Z, R1, R
      COMMON /C3/A, G
      COMMON /C4/RO, DZ
      COMMON Y, PRO, AL, D, R2, AJO, AN, DX
      COMMON GX(201), PX(2, 201), PX2(2, 201)
      SR=(R1**2+Y**2-2.0*R1*Y*COS(TH))**0.5
      IF(R.EQ.0.0) GO TO 10
      XX=SR/R
      J=1+IFIX((XX-1.0)/DX)
      R2=RO**2
      RSO=PS(0.0)
      PA=PSO*GX(J)*(R2-AL*AJO*R**2)/AJO/R**2*(1.0+(PX(1, J)+AL*PX2(1, J))
     1   *AJO*R**2/(R2-AL*AJO*R**2))
      FP=PA*COS(TH)
   10 IF(R.EQ.0.0) FP=PS(0.0)
      RETURN
      END


      FUNCTION PS(TH)
      COMMON Y, PRO, AL, D, R2, AJO, AN, DX
      COMMON /C2/Z, R1, R
      COMMON /C3/A, G
      COMMON /C4/RO, DZ
      COMMON /C5/PO1
      PP=PO1*(1.0+(G-1.0)/2.0*AN**2)**(G/(1.0-G))
      PS=PP*COS(TH)
      RETURN
      END


      SUBROUTINE G1
      DIMENSION YO(2), Y3(2), YY3(2), HX(201)
      COMMON /BB/H, XO
      COMMON Y, PRO, AL, D, R2, AJO, AN, DX
      COMMON GX(201), PX(2, 201), PX2(2, 201)
      COMMON /C/ZZ(201)
      COMMON /C1/Y4(2, 301)
      COMMON /C3/A, G
      H=DX
      XO=1.0
      D=H
      NX=IFIX(1.0/(-H)+1
      YO(1)=2.0/(G+1.0)
      YO(2)=(G+1.0)/2.0/G
      Y1=(G+1.0)/(G-1.0)
      Y2=2.0*G/(G+1.0)
      Y3(1)=-(G-1.0)/2.0/G
      Y3(2)=-2.0/(G-1.0)
      YY3(1)=0.0
      YY3(2)=0.0
      EXTERNAL Q, F1, F2, F3, F4
      NN=3*NX-2
      H=H/3.0
      CALL RKGN(XO, YO, Y4, H, NN, 2, Q)
      DO 100 I=1, NN
```

```
100 ZZ(I)=
  1   (A+1.0)/(1.0+H*FLOAT(I-1)-Y4(1, I))
      CALL RKG(XO, Y1, HX, D, NX, F1)
      CALL RKG(XO, Y2, GX, D, NX, F2)
      CALL RKGN (XO, Y3, PX, D, NX, 2, F3)
      CALL RKGN(XO, YY3, PX2, D, NX, 2, F4)
      DO 115 I=1, NX
      Y4(1, I)=Y4(1, 3*I-2)
115   Y4(2, I)=Y4(2, 3*I-2)
      Y4(1, NX)=Y4(1, NX-1)
      Y4(2, NX)=Y4(2, NX-1)
      HX(NX)=HX(NX-1)
      GX(NX)=GX(NX-1)
      PX(1, NX)=PX(1, NX-1)
      PX(2, NX)=PX(2, NX-1)
      PX2(1, NX)=PX2(1, NX-1)
      PX2(2, NX)=PX2(2, NX-1)
      RETURN
      END

      SUBROUTINE SMACH (AM, G, E)
      AM=1.0+0.35*E
10    CONTINUE
      AMO=AM
      X=2.0/(G+1.0)*(1.0+(G-1.0)/2.0*AM**2)
      AM=AM-(X**((G+1.0)/2.0/(G-1.0))/AM-E)/X**((G+1.0)/2.0/(G-1.0))
  1   /(1.0/X-1.0/AM**2)
      IF(ABS(AMO-AM)/AM.GT.1.0E-06) GO TO 10
      RETURN
      END

      FUNCTION Q(K, X, Y)
      DIMENSION Y(8)
      COMMON/C3/A, G
      GO TO (1, 2), K
1 Q       =((A+1.0)/G-A*Y(1)/X+(A+1.0)/2.0*Y(2)*Y(1))/(1.0-(X-Y(1))
  1   *Y(2))
      GO TO 3
2 Q       =(A+2.0-G*((A+1.0)/G-A*Y(1)/X+(A+1.0)/2.0*Y(2)*Y(1))/
  1   (1.0-(X-Y(1))*Y(2))-A*(G-1.0)/X*Y(1))/(X-Y(1))*Y(2)
3 RETURN
      END

      FUNCTION F1(X, Y)
      COMMON /C3/A, G
      F1=Y*(YX(X)+A*YY1(X)/X)/(X-YY1(X))
      RETURN
      END

      FUNCTION F2(X, Y)
      COMMON /C3/A, G
      F2=Y*(G*YX(X)+A*G*YY1(X)/X-A-1.0)/(X-YY1(X))
      RETURN
      END

      FUNCTION YY1(X)
```

```
      COMMON /BB/H, XO
      COMMON /C1/Y4(2, 301)
      I=1-IFIX((XO+0.0001-X)/H)
      YY1=Y4(1, I)
      RETURN
      END

      FUNCTION YY2(X)
      COMMON /BB/H,XO
      COMMON /C1/Y4(2, 301)
      I=1-IFIX((XO+0.0001-X)/H)
      YY2=Y4(2, I)
      RETURN
      END

      FUNCTION YX(X)
      COMMON /C3/A, G
      YX=((A+1.0)/G-A*YY1(X)/X+(A+1.0)/2.0*YY2(X)*YY1(X))/(1.0-(X-YY1(X)
     1 )*YY2(X))
      RETURN
      END

      FUNCTION F3(K, X, Y)
      COMMON /C3/A, G
      DIMENSION Y(2)
      GO TO (1, 2), K
    1 F3=P1(X)*Y(2)+P2(X)*Y(1)-YY2(X)/(1.0-(X-YY1(X))*YY2(X))*(3.0*G-
     1 1.0)/(2.0*G-1.0)*(G+1.0)/(G-1.0)*(YX(X)+(A+1.0)/2.0*YY1(X)/
     2 (X-YY1(X)))*E(X)
      RETURN
    2 F3=(P1(X)*Y(2)+P2(X)*Y(1)-YY2(X)/(1.0-(X-YY1(X))*YY2(X))*(3.0*G-
     1 1.0)/(2.0*G-1.0)*(G+1.0)/(G-1.0)*(YX(X)+(A+1.0)/2.0*YY1(X)/
     2 (X-YY1(X)))*E(X))/G-(A+1.0)/G/(X-YY1(X))*((G-1.0)*Y(2)+Y(1))
      RETURN
      END

      FUNCTION F4(K, X, Y)
      COMMON /C3/A, G
      DIMENSION Y(2)
      GO TO (1, 2), K
    1 F4=P1(X)*Y(2)+P2(X)*Y(1)+YY2(X)/(1.0-(X-YY1(X))*YY2(X))*(-2.0*G
     1 /(2.0*G-1.0)*(YX(X)+(A+1.0)/2.0*YY1(X)/(X-YY1(X)))*(1.0-E(X))
     2 +(A+1.0)/2.0*G*YY1(X)/(X-YY1(X))+A+1.0)
      RETURN
    2 R4=(P1(X)*Y(2)+P2(X)*Y(1)+YY2(X)/(1.0-(X-YY1(X))*YY2(X))*(-2.0*G
     1 /(2.0*G-1.0)*(YX(X)+(A+1.0)/2.0*YY1(X)/(X-YY1(X)))*(1.0-E(X))
     2 +(A+1.0)/2.0*G*YY1(X)/(X-YY1(X))+A+1.0))/G-(A+1.0)/G/(X-YY1(X))
     3 *((G-1.0)*Y(2)+Y(1)-1.0)
      RETURN
      END

      FUNCTION P1(X)
      COMMON /C3/A, G
      P1=-YY2(X)/(1.0-(X-YY1(X))*YY2(X))*(2.0*G*YX(X)+(A-1.0)/2.0*G
     1 +G/(2.0*G-1.0)*(YX(X)+(A+1.0)/2.0*YY1(X)/(X-YY1(X)))+(A+1.0)*(G
     2 -1.0))
```

```
      RETURN
      END

      FUNCTION P2(X)
      COMMON /C3/A, G
      P2=YY2(X)/(1.0-(X-YY1(X))*YY2(X))*(G*(3.0-2.0*G)/(2.0*G-1.0)
     1  *(YX(X)+(A+1.0)/2.0*YY1(X)/(X-YY1(X)))-A-1.0)
      RETURN
      END

      FUNCTION E(B)
      COMMON /BB/H, XO
      COMMON /C/ZZ(201)
      E=EXP(SEKBN3(ZZ, H, IFIX((XO-B)/(-H))+1))
      RETURN
      END
```

2.2   SHOCK WAVE (two-dimension forward-facing step)

```
            HARP 5020 COMPILED LIST
                EXTERNAL FORMULA NUMBER—SOURCE STATEMENT
      AJO=0.877
      AJ1=-1.989
      AM=2.558
   10 V=-AJO*AL1*RRO
      AK=(-AJO*AL1)**(-1.5)*(SQRT(V*(1.0+V))-ALOG(SQRT(1.0+V)+SQRT(V)))
      XRO=AM*SQRT(AJO)*AK
      RRO=RRO+0.5
      WRITE (6, 100) XRO, RRO
  100 FORMAT(1H , 2F15.5)
      IF(RRO.LT.12.0) GO TO 10
      STOP
      END
```

2.3 J_0 and λ

```
            HARP 5020 COMPILED LIST
                EXTERNAL FORMULA NUMBER—SOURCE STATEMENT
      DIMENSION YO(2), Y3(2), YY3(2), XX(201), X1(201), X2(201), SJ(201),
     1  HX(201), GX(201), PX(2, 201), PX2(2, 201), S(201), T(201),
     2  PH(201), PS(201), XA(201)
      COMMON A, G/,BB/H, XO
      COMMON /C/Z(201)
      COMMON /C1/Y4(2, 201)
      READ(5, 1)A, G, H, XO
    1 FORMAT(4F10.3)
      WRITE(6, 2)A, G, H
    2 FORMAT(1H , 3X6HALPHA=, F5.3, 3X, 6HGAMMA=, F5.3, 3X, 3HDX=, F6.3///
     1  3X1HX, 9X, 1HF, 13XIHD, 13X, IHH, 13X1HG, 11X, 5HPSAI1, 9X, 5HPHAI1, 9X,
     2  5HPSAI2, 9X, 5HPHAI2)
      D=H
      NX=IFIX(1.0/(-H))+1
      YO(1)=2.0/(G+1.0)
      YO(2)=(G+1.0)/2.0/G
      Y1    =(G+1.0)/(G-1.0)
      Y2    =2.0*G(G+1.0)
      Y3(1)=-(G-1.0)/2.0/G
```

```
        Y3(2)=-2.0/(G-1.0)
        YY3(1)=0.0
        YY3(2)=0.0
        DO 110 I=1, NX
110 XX(I)=XO+H*FLOAT(I-1)
        EXTERNAL Q, F1, F2, F3, F4
        NN=2*NX-1
        H=H/2.0
        CALL RKGN (XO, YO, Y4, H, NN, 2, Q)
        DO 100 I=1, NN
100 ZZ(I)=(A+1.0)/(1.0+H*FLOAT(I-1)-Y4(1, I))
        CALL RKG(XO, Y1, HX, D, NX, F1)
        CALL RKG(XO, Y2, GX, D, NX, F2)
        CALL RKGN(XO, Y3, PX, D, NX, 2, F3)
        CALL RKGN(XO, YY3, PX2, D, NX, 2, F4)
        DO 115 I=1, NX
        Y4(1, I)=Y4(1,2*I-1)
115 Y4(2, I)=Y4(2, 2*I-1)
        Y4(1, NX)=Y4(1, NX-1)
        Y4(2, NX)=Y4(2, NX-1)
        HX(NX)=HX(NX-1)
        GX(NX)=GX(NX-1)
        PX(1, NX)=PX(1, NX-1)
        PX(2, NX)=PX(2, NX-1)
        PX2(1, NX)=PX2(1, NX-1)
        PX2(2, NX)=PX2(2, NX-1)
        WRITE (6, 10)(XX(I), Y4(1, I), Y4(2, I), HX(I), GX(I), PX(1, I), PX(2, I),
     1  PX2(1, I), PX2(2, I), I=1, NX)
10  FORMAT(1H , F6.3, 8E14.5)
        DO 121 I=1, NX
        X1(I)=(-PX(2, I)+2.0*PX(1, I)-(3.0*G-1.0)/G*(G+1.0)/(G-1.0)*E(XX(I)))
     1  /(2.0*G-1.0)
        X2(I)=(-PX2(2, I)+2.0*PX2(1, I)+2.0
     1  *E(XX(I))-2.0)/(2.0*G-1.0)
        S(I)=(G*Y4(1, I)*(XX(I)-Y4(1, I))*HX(I)*PX(2, I)+GX(I)/(G-1.0)*PX
     1  (1, I)+G/2.0*Y4(1, I)**2*HX(I)*X1(I))*XX(I)**A
        T(I)=(G*Y4(1, I)*(XX(I)-Y4(1, I))*HX(I)*PX2(2, I)+GX(I)/(G-1.0)
     1  *PX2(1, I)+G/2.0*Y4(1, I)**2*HX(I)*X2(I))*XX(I)**A
121 CONTINUE
        SS=SEKBN3(S, -D, NX)
        ST=SEKBN3(T, -D, NX)
        DO 130 I=1, NX
130 SJ(I)=(G/2.0*HX(I)*Y4(1, I)**2+GX(I)/(G-1.0))*XX(I)**A
        AJO=SEKBN3(SJ, -D, NX)
        ALAMDA=(SS-1.0/(G-1.0)/(A+1.0))/(AJO-ST)
        WRITE (6, 55)AJO, ALAMDA
55  FORMAT(1H0, 9X, 3HJO=, F8.5/6X, 7HLAMDA1=, F8.5)
        DO 140 I=1, NX
        PH(I)=PX(2, I)+ALAMDA*PX2(2, I)
        PS(I)=PX(1, I)+ALAMDA*PX2(1, I)
140 XA(I)=X1(I)+ALAMDA*X2(I)
        WRITE (6, 60)
60  FORMAT (1H1, 3X, 1HX, 5X, 4HPHAI, 6X, 4HPSAI, 7X, 3HXAI)
        WRITE (6, 65) (XX(I), PH(I), PS(I), XA(I), I=1, NX)
65  FORMAT (1H , F6.3, 3F18.5)
```

```
      STOP
      END

      FUNCTION Q(K, X, Y)
      DIMENSION Y(8)
      COMMON A, G
      GO TO (1, 2), K
1 Q        =((A+1.0)/G−A*Y(1)/X+(A+1.0)/2.0*Y(2)*Y(1))/(1.0−(X−Y(1))
  1    *Y(2))
      GO TO 3
2 Q        =(A+2.0−G*((A+1.0)/G−A*Y(1)/X+(A+1.0)/2.0*Y(2)*Y(1))/
  1    (1.0−(X−Y(1))*Y(2))−A*(G−1.0)/X*Y(1))/(X−Y(1))Y*(2)
3 RETURN
      END

      FUNCTION F1(X, Y)
      COMMON A, G
      F1=Y*(YX(X)+A*YY1(X)/X)/(X−YY1(X))
      RETURN
      END

      FUNCTION F2(X, Y)
      COMMON A, G
      F2=Y*(G*YX(X)+A*G*YY1(X)/X−A−1.0)/(X−YY1(X))
      RETURN
      END

      FUNCTION YY1(X)
      COMMON /BB/H, XO
      COMMON /C1/Y4(2, 201)
      I=1−IFIX((XO+0.0001−X)/H)
      YY1=Y4(1, I)
      RETURN
      END

      FUNCTION YY2(X)
      COMMON /BB/H, XO
      COMMON /C1/Y4(2, 201)
      I=1−IFIX((XO+0.0001−X)/H)
      YY2=Y4(2, I)
      RETURN
      END

      FUNCTION YX(X)
      COMMON A,'G
      YX=((A+1.0)/G−A*YY1(X)/X+(A+1.0)/2.0*YY2(X)*YY1(X))/(1.0−(X−YY1(X)
  1    )*YY2(X))
      RETURN
      END

      FUNCTION F3(K, X, Y)
      COMMON A, G
      DIMENSION Y(2)
      GO TO (1, 2), K
1 F3=P1(X)*Y(2)+P2(X)*Y(1)−YY2(X)/(1.0−(X−YY1(X))*YY2(X))*(3.0*G−
  1    1.0)/(2.0*G−1.0)*(G+1.0)/(G−1.0)*(YX(X)+(A+1.0)/2.0*YY1(X)/
  2    (X−YY1(X)))*E(X)
```

```
      RETURN
    2 F3=(P1(X)*Y(2)+P2(X)*Y(1)-YY2(X)/(1.0-(X-YY1(X))*YY2(X))*(3.0*G-
    1   1.0)/(2.0*G-1.0)*(G+1.0)/(G-1.0)*(YX(X)+(A+1.0)/2.0*YY1(X)/
    2   (X-YY1(X)))*E(X))/G-(A+1.0)/G/(X-YY1(X))*((G-1.0)*Y(2)+Y(1))
      RETURN
      END

      FUNCTION F4(K, X, Y)
      COMMON A, G
      DIMENSION Y(2)
      GO TO (1, 2), K
    1 F4=P1(X)*Y(2)+P2(X)*Y(1)+YY2(X)/(1.0-(X-YY1(X))*YY2(X))*(-2.0*G
    1   /(2.0*G-1.0)*(YX(X)+(A+1.0)/2.0*YY1(X)/(X-YY1(X)))*(1.0-E(X))
    2   +(A+1.0)/2.0*G*YY1(X)/(X-YY1(X))+A+1.0)
      RETURN
    2 F4=(P1(X)*Y(2)+P2(X)*Y(1)+YY2(X)/(1.0-(X-YY1(X))*YY2(X))*(-2.0*G
    1   /(2.0*G-1.0)*(YX(X)+(A+1.0)/2.0*YY1(X)/(X-YY1(X)))*(1.0-E(X))
    2   +(A+1.0)/2.0*G*YY1(X)/(X-YY1(X))+A+1.0))/G-(A+1.0)/G/(X-YY1(X))
    3   *((G-1.0)*Y(2)+Y(1)-1.0)
      RETURN
      END

      FUNCTION P1(X)
      COMMON A, G
      P1=-YY2(X)/(1.0-(X-YY1(X))*YY2(X))*(2.0*G*YX(X)+(A-1.0)/2.0*G
    1   +G/(2.0*G-1.0)*(YX(X)+(A+1.0)/2.0*YY1(X)/(X-YY1(X)))+(A+1.0)*(G
    2   -1.0))
      RETURN
      END

      FUNCTION P2(X)
      COMMON A, G
      P2=YY2(X)/(1.0-(X-YY1(X))*YY2(X))*(G*(3.0-2.0*G)/(2.0*G-1.0)
    1   *(YX(X)+(A+1.0)/2.0*YY1(X)/(X-YY1(X)))-A-1.0)
      RETURN
      END
```
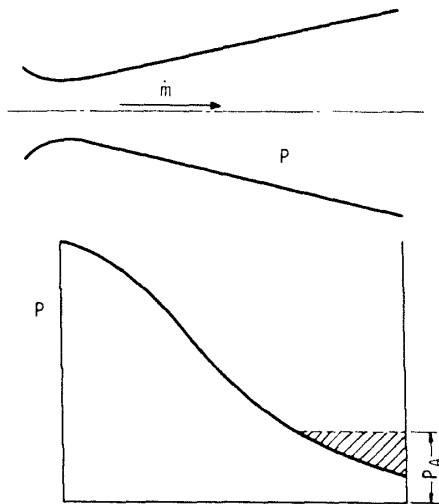
Fig. 1 Pressure distribution on a rocket nozzle axis
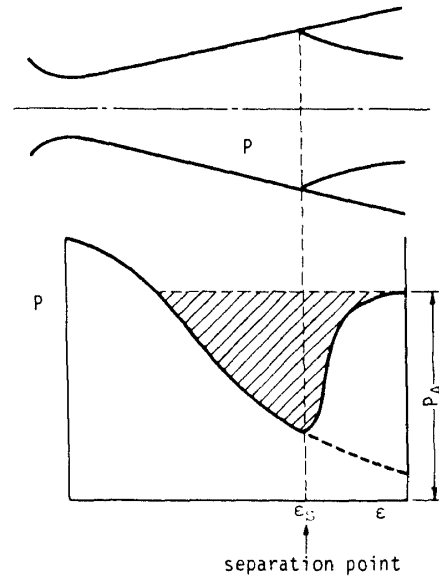
Fig. 2 Pressure distribution of a boundary layer separation
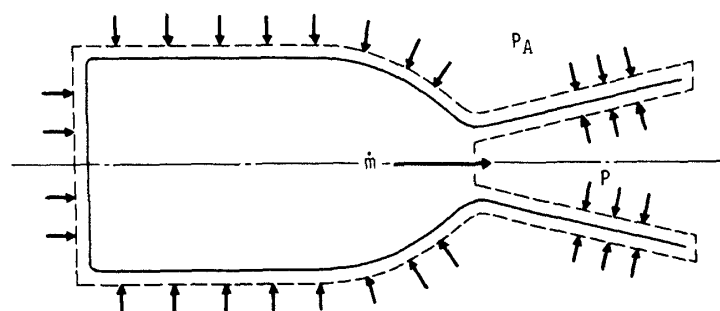
Fig. 3 Mechanism of thrust producing
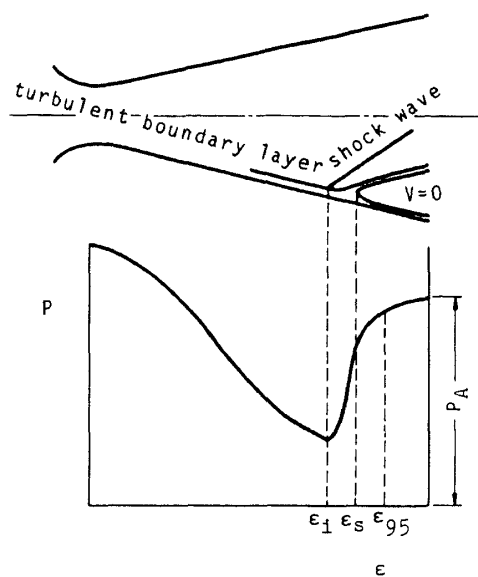
Fig. 4 Flow field of boundary layer separation and
pressure distribution
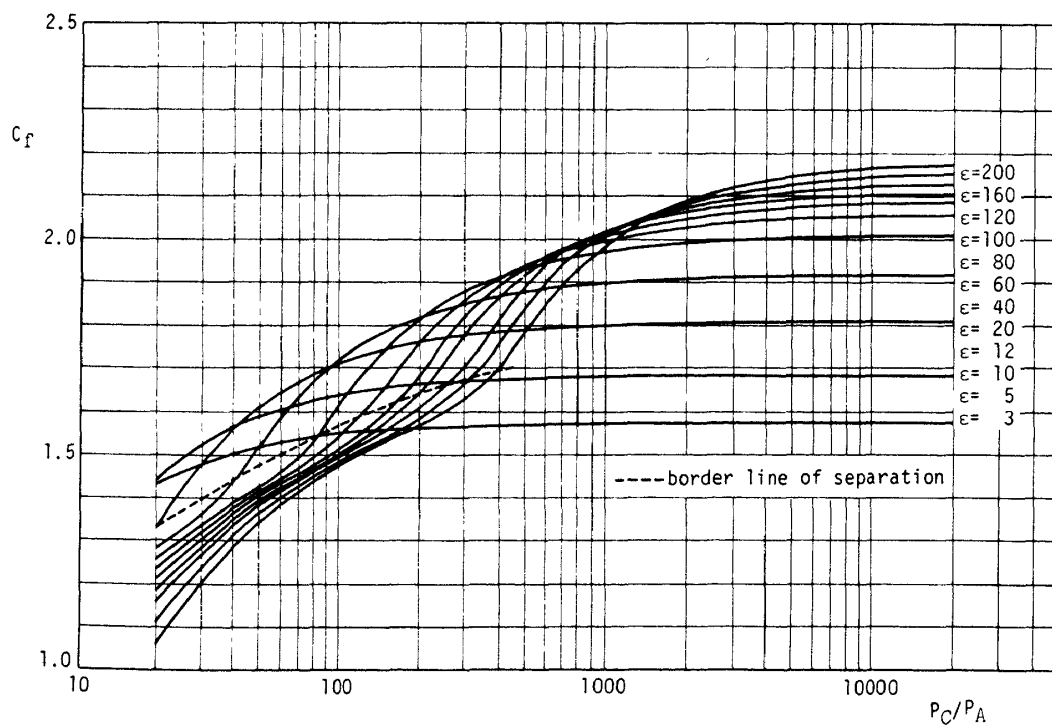
Fig. 5 Characteristics of C_f (γ = 1.10)
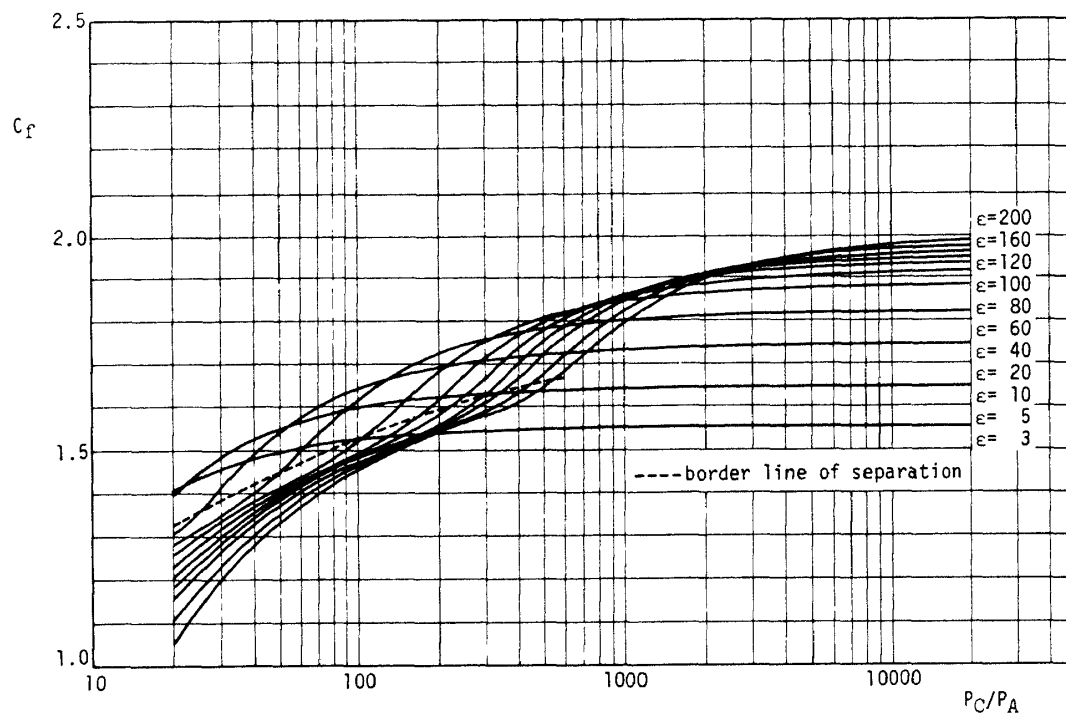
Fig. 6 Characteristics of C_f (γ = 1.20)
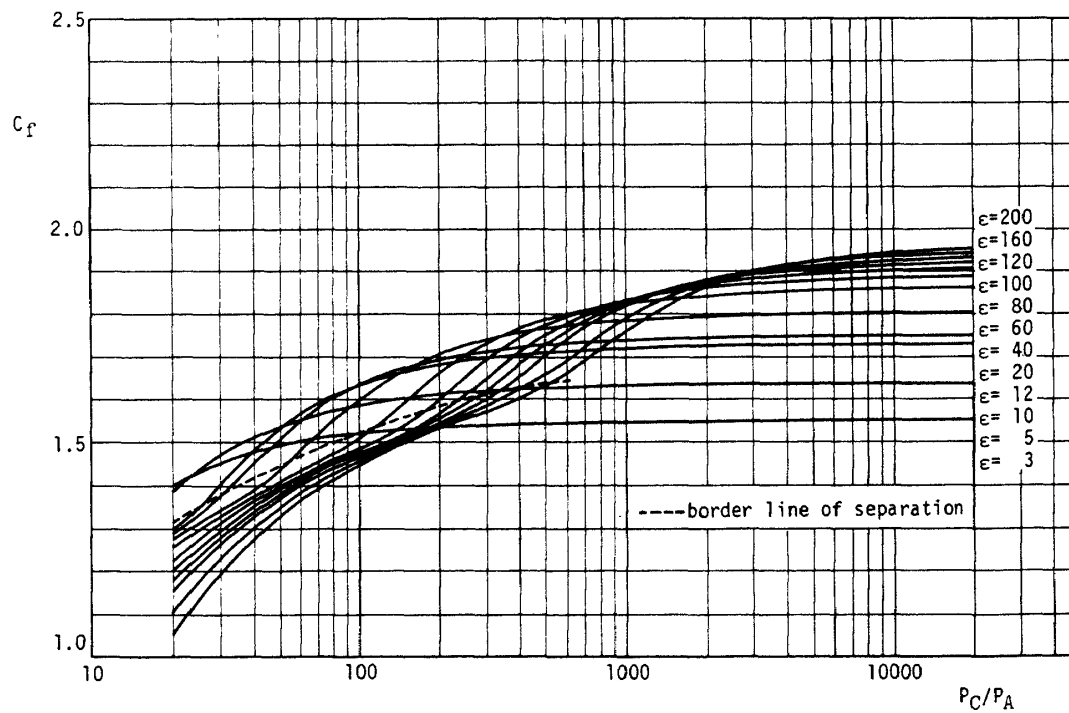
Fig. 7 Characteristics of C_f (γ = 1.22)
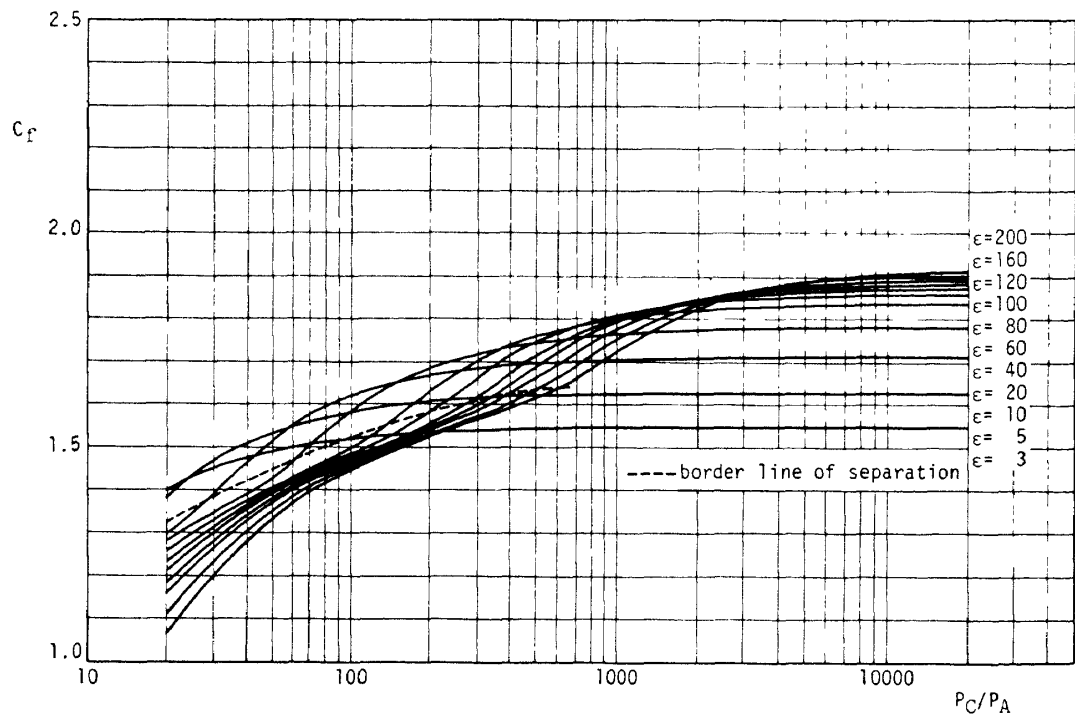
Fig. 8 Characteristics of C_f (γ = 1.25)

Fig. 9 Characteristics of C_f (γ = 1.30)

Test No.	ε	Nozzle material
1	3.38	S U S
2	6.0	F R P
3	8.0	S U S
4		F R P
5	12.0	S U S
6		F R P
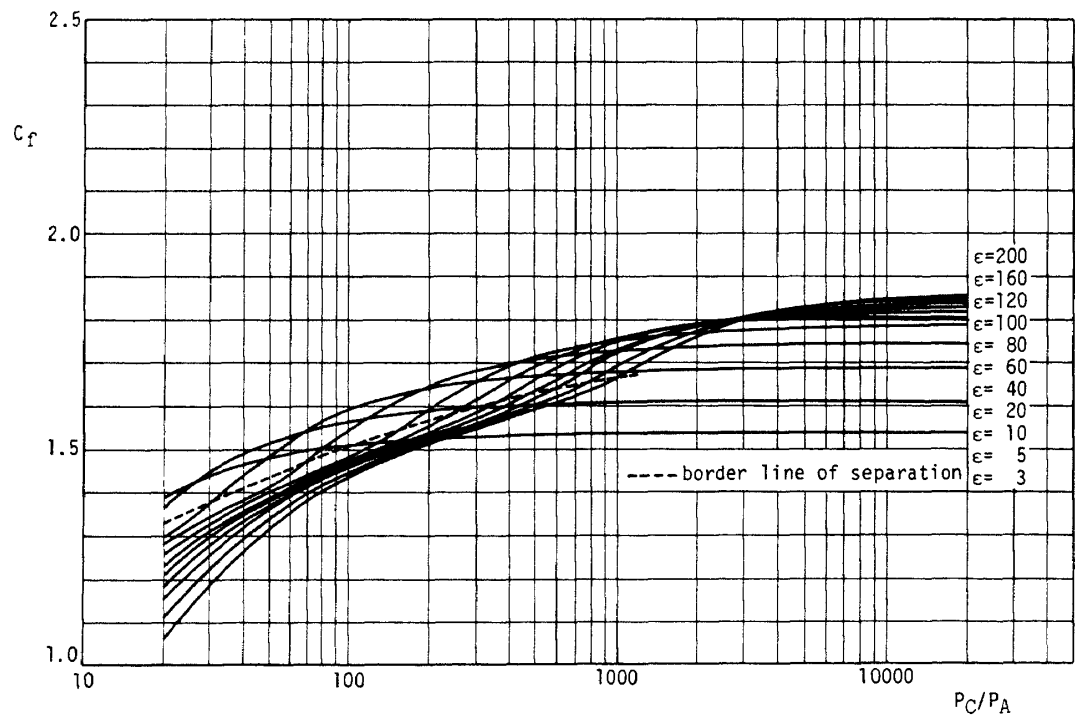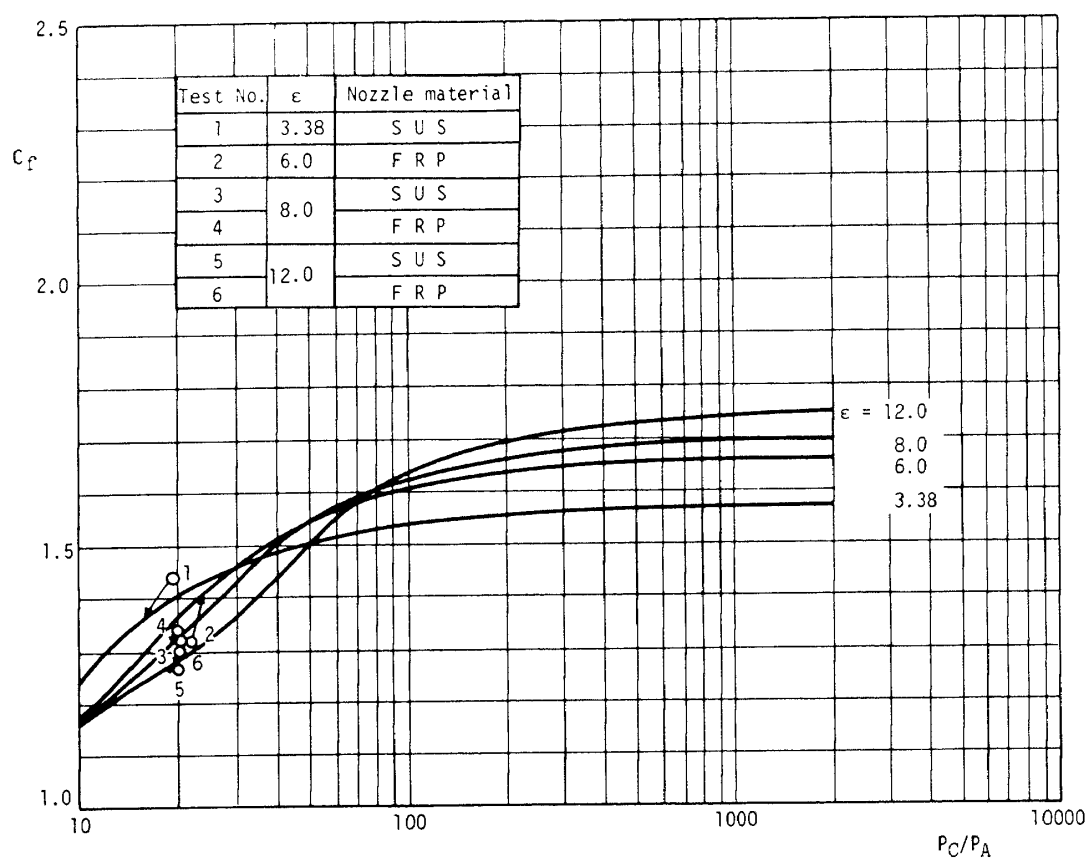
Fig.10 Measured thrust coefficient at sea level (γ = 1.22)
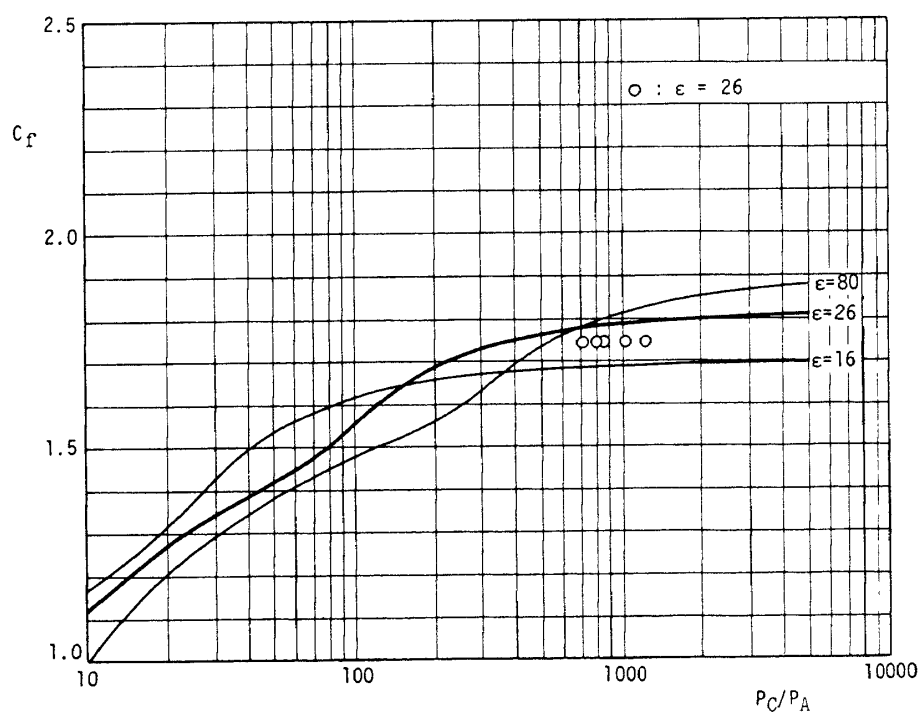
Fig.11 Measured thrust coefficient at low ambient pressure
(γ = 1.235)
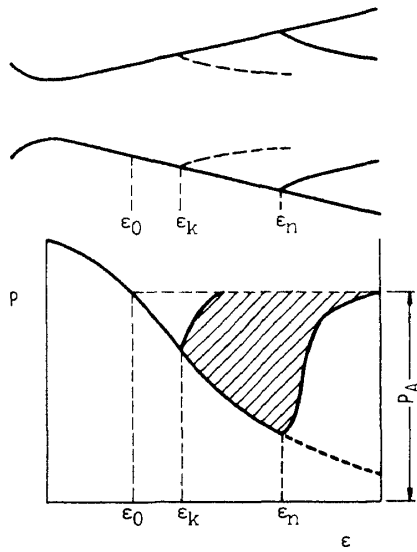
Fig.12 Forced separation position ε_k
and pressure distribution
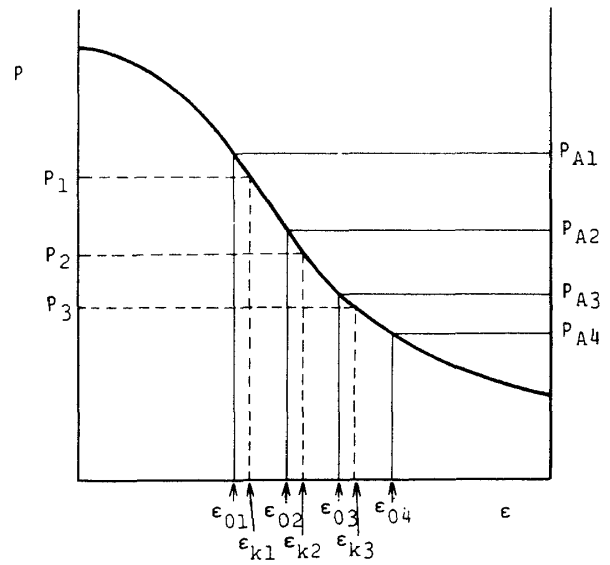
Fig.13 Arrengement of ε_{ki} ($i = 1,2,\cdots,n$)
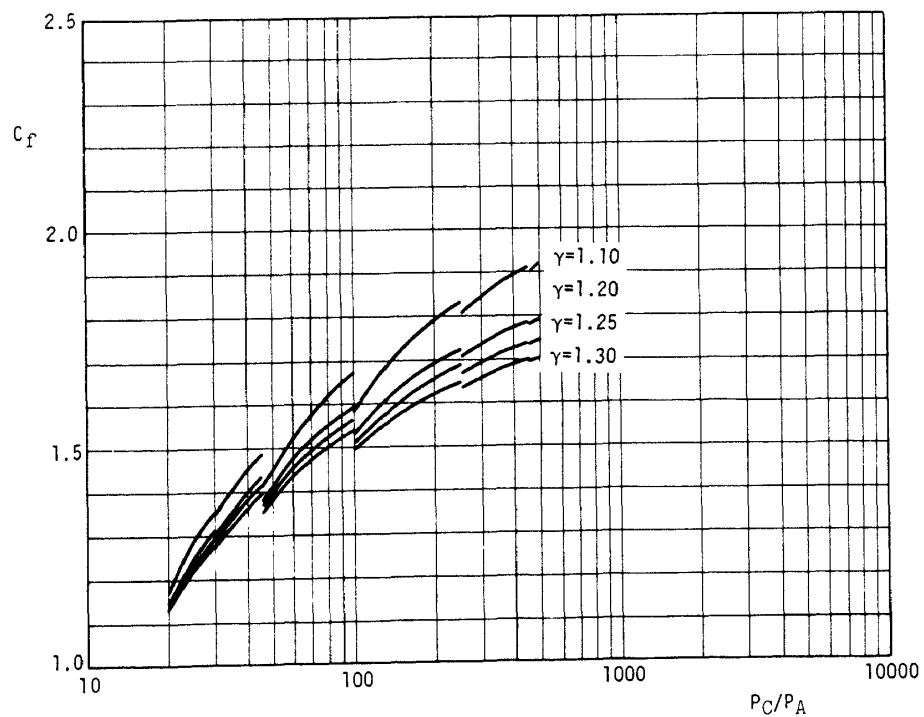
Fig.14 Characteristics of C_f with separation position control
($Pc = 20$ kg/cm^2, $\varepsilon = 200$)
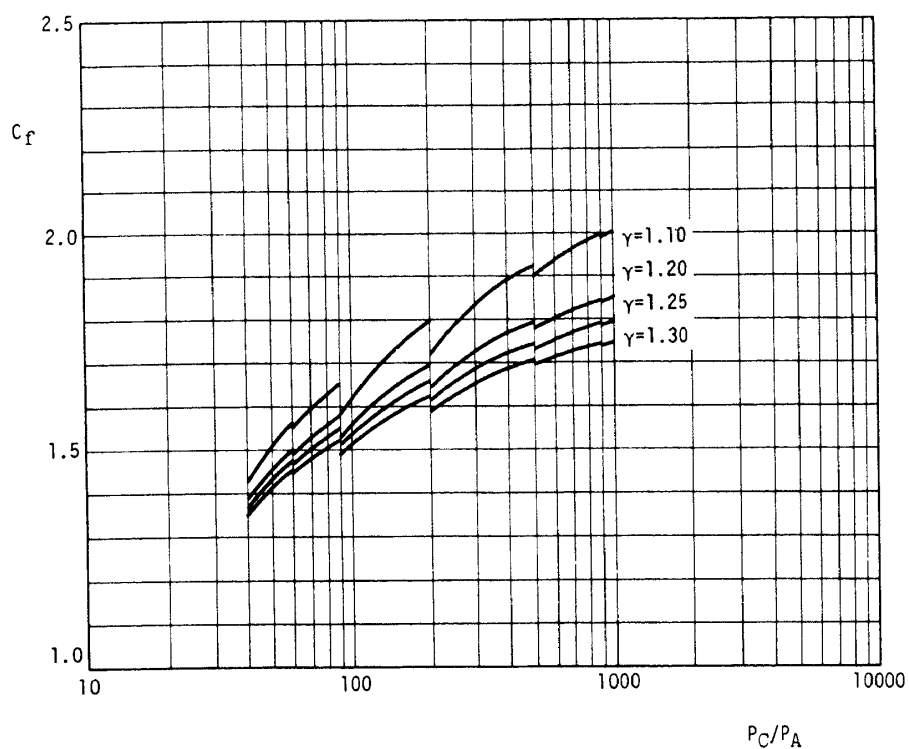
Fig.15 Characteristics of C_f with separation position control
(Pc = 40 kg/cm², ε = 200)
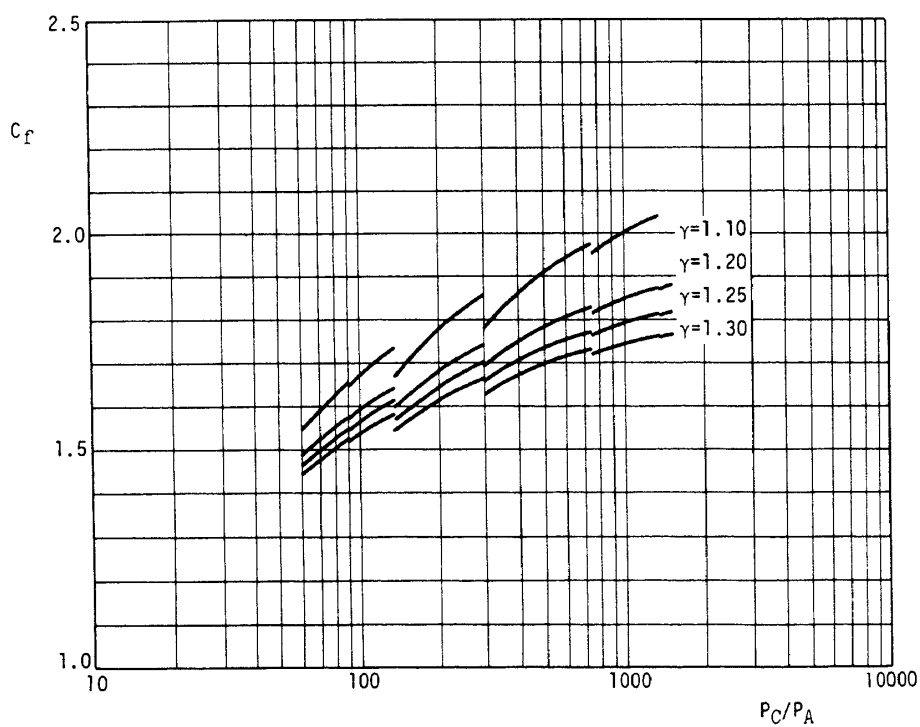
Fig.16 Characteristics of C_f with separation position control
(Pc = 60 kg/cm², ε = 200)
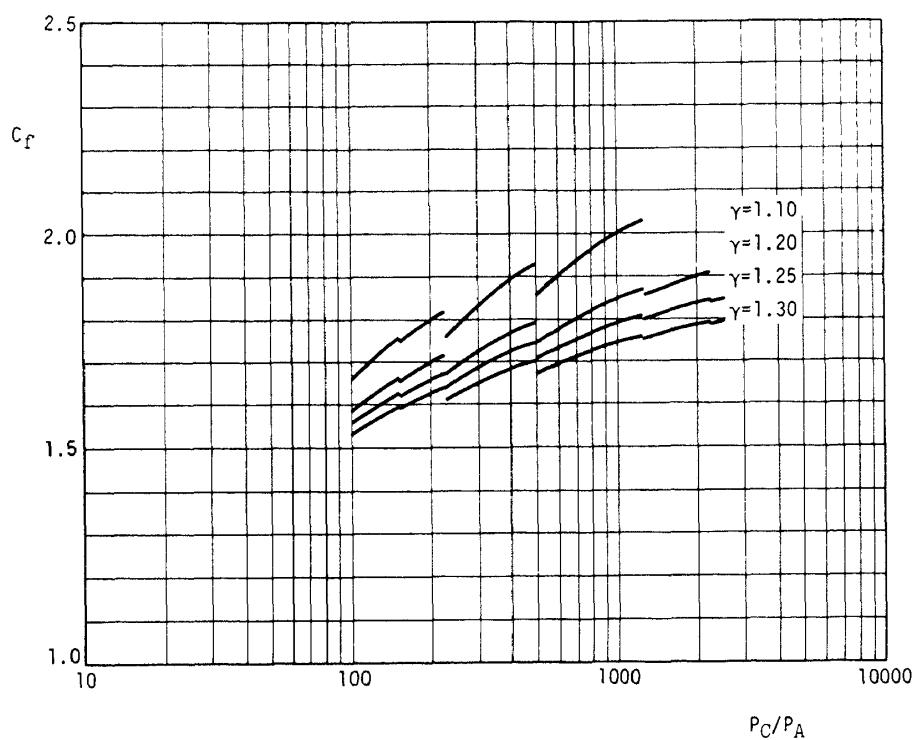
Fig.17 Characteristics of C_f with separation position control
(Pc = 100 kg/cm², ε = 200)
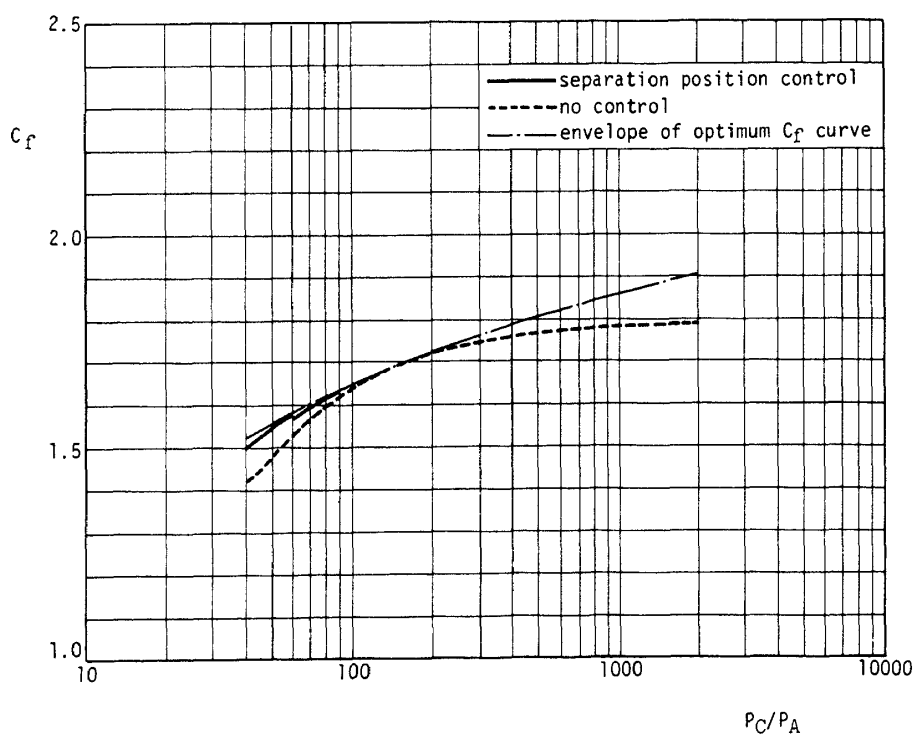
Fig.18 Characteristics of C_f with separation position control
(Pc = 40 kg/cm², γ = 1.20 , ε = 16)
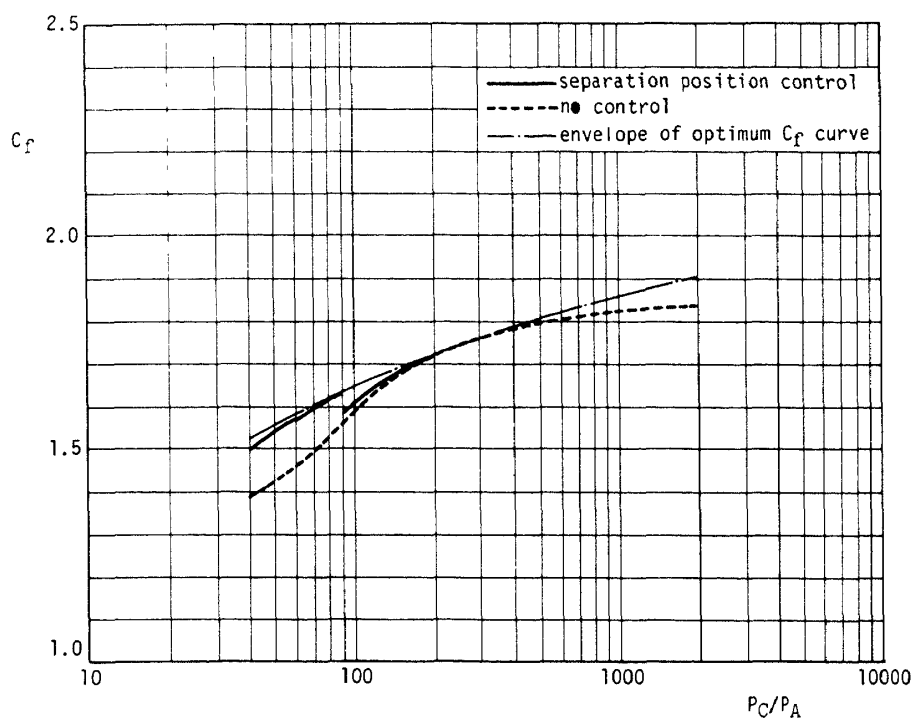
Fig.19 Characteristics of C_f with separation position control

(Pc = 40 kg/cm^2, γ = 1.20 , ϵ = 26)
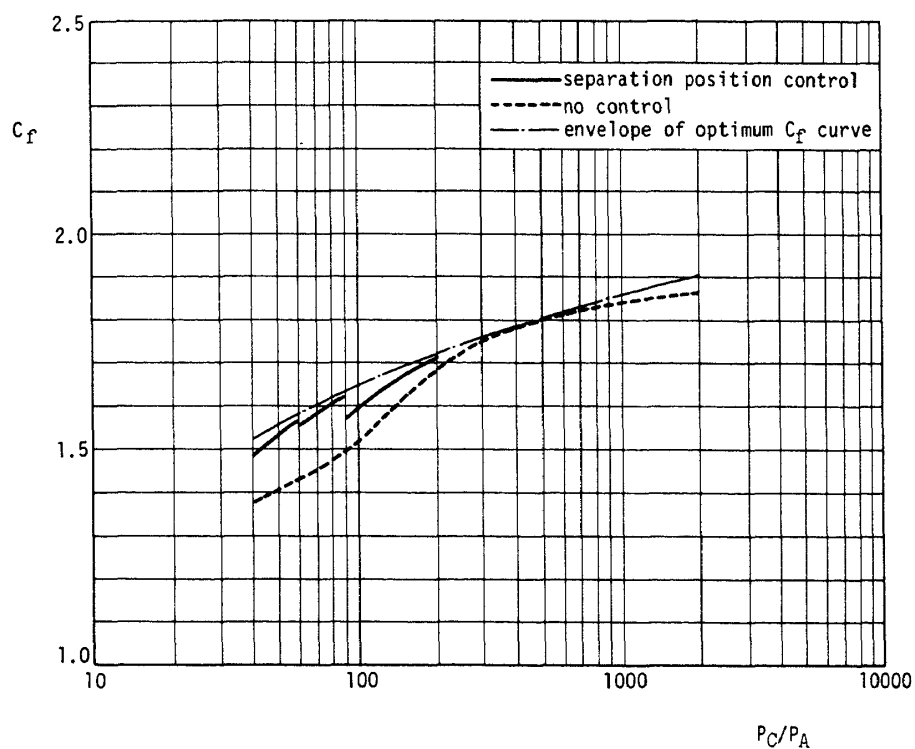
Fig.20 characteristics of C_f with separation position control

(Pc = 40 kg/cm^2, γ = 1.20 , ϵ = 40)
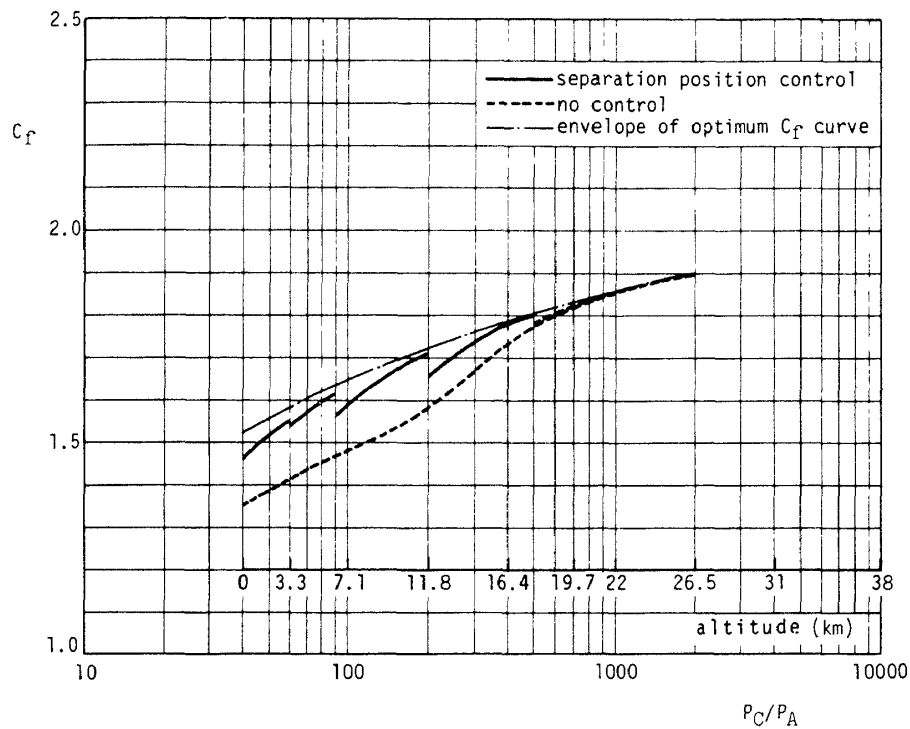
Fig.21 Characteristics of C_f with separation position control

(Pc = 40 kg/cm², γ = 1.20 , ε = 80)

Table 1   300kg thrust liquid propellant rocket engine C_f measurement

(LOX-C_2H_5·OH , γ = 1.22)

Test No.	ε	Nozzle material	F kg	P_A kg/cm²	P_C/P_A	C_f(expe.)	C_f(theo.)	η %
1	3.38	S U S	308	1.04	19.1	1.439	1.399	102.9
2	6.0	F R P	286	1.05	19.6	1.304	1.352	96.5
3	8.0	S U S	284	1.04	19.2	1.321	1.314	100.5
4		F R P	287	1.04	19.2	1.335	1.314	101.6
5	12.0	S U S	270	1.04	19.1	1.262	1.280	98.6
6		F R P	282	1.05	19.2	1.311	1.280	102.4

Table 2   LE-3 rocket engine C_f measurement   (N_2O_4-A·50 , ε = 26)

Test No.	A_t cm²	$Pc(inj)$ kg/cm²	P_A kg/cm²	$Pc(inj)/P_A$	O/F	γ	F kg	C_f (expe.)	C_f (theo.)	η %
KT-017	268.72	11.75	$\times 10^{-2}$ 1.373	855.9	1.496	1.235	5502	1.743	1.785	97.65
KT-028	268.72	11.78	0.965	1220.7	1.510	1.235	5519	1.743	1.795	97.10
KT-029	268.72	11.75	1.155	1017.0	1.504	1.235	5516	1.747	1.791	97.54
KT-034	268.18	11.74	1.454	807.2	1.522	1.235	5502	1.741	1.784	97.59
KT-039	268.18	11.74	1.645	713.8	1.517	1.235	5502	1.741	1.780	97.81
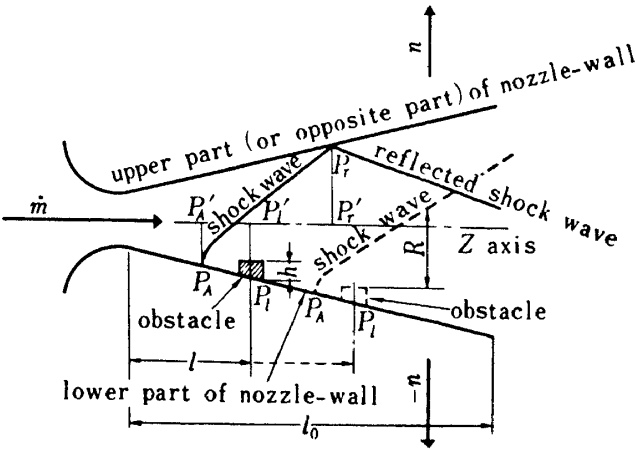
Fig.22 Shock waves induced by obstacles
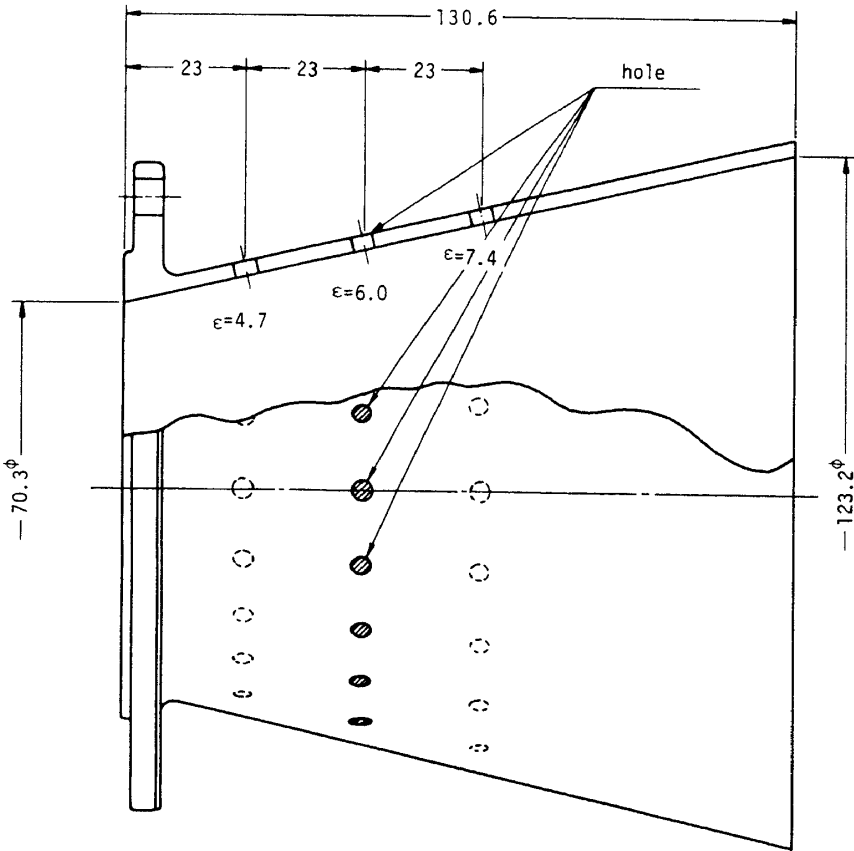
Fig.23 Overexpanded nozzle
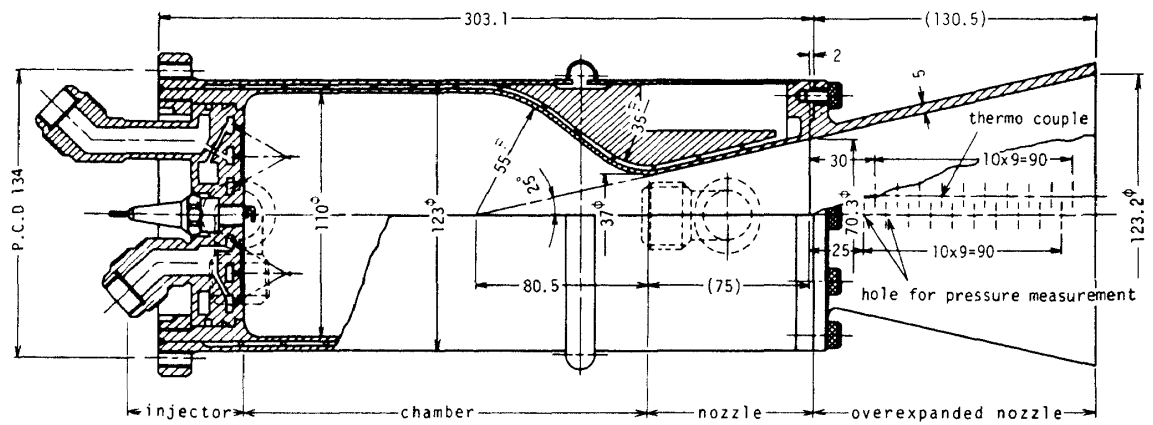
Fig.24 Rocket engine
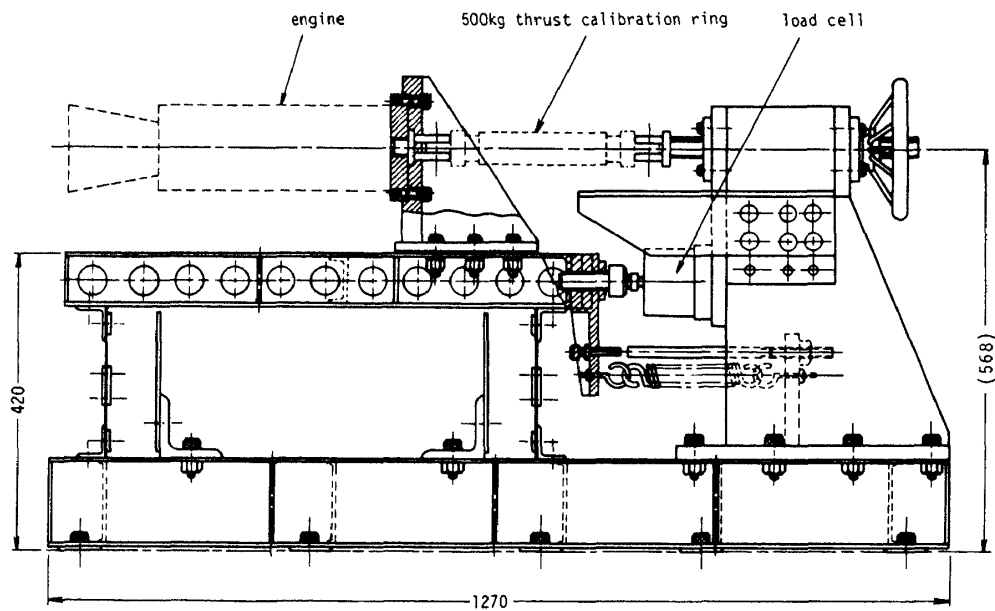
Fig.25 Test stand
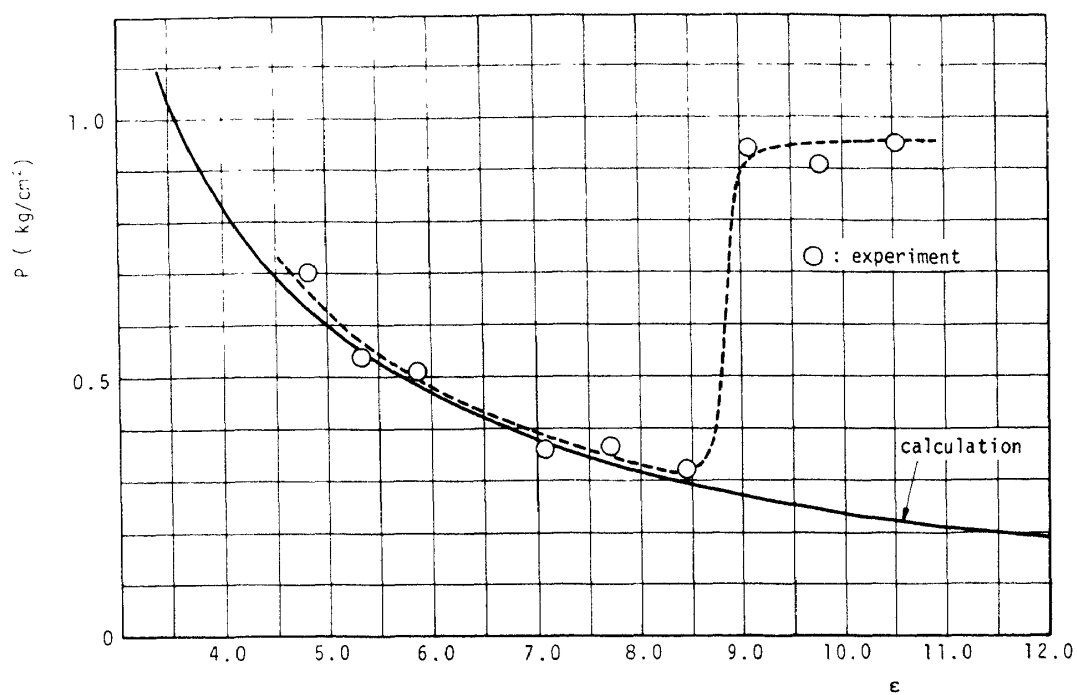
Fig.26 Pressure distribution measurement (Pc = 19.8 kg/cm², ε = 12 , γ = 1.22)
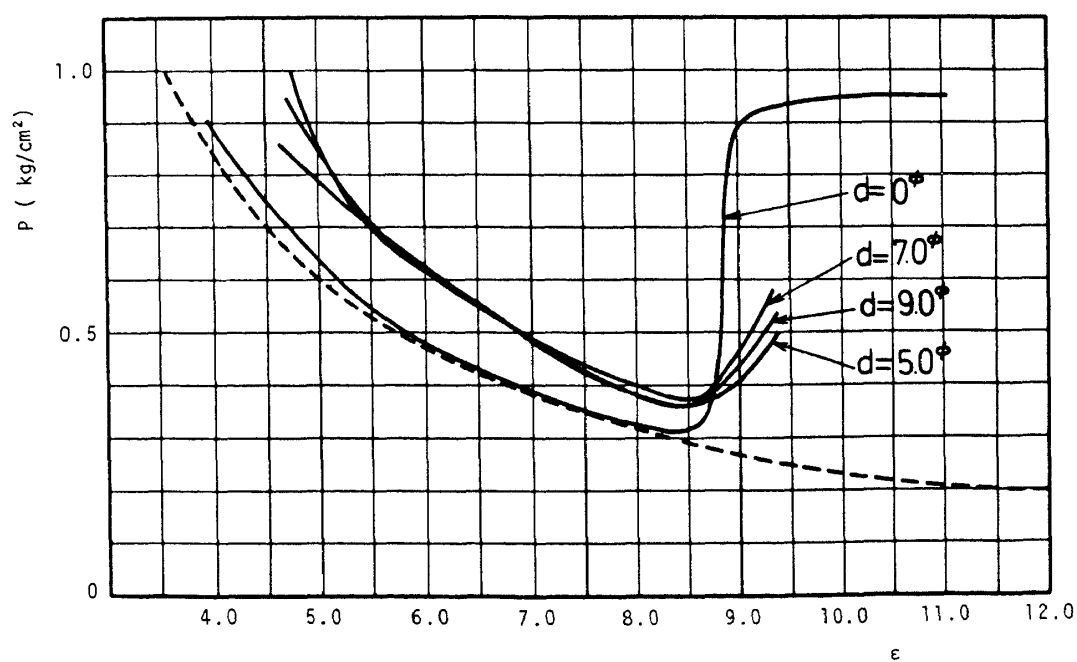
Fig.27 Pressure distribution measurement on the nozzle wall with hole at ε = 4.7
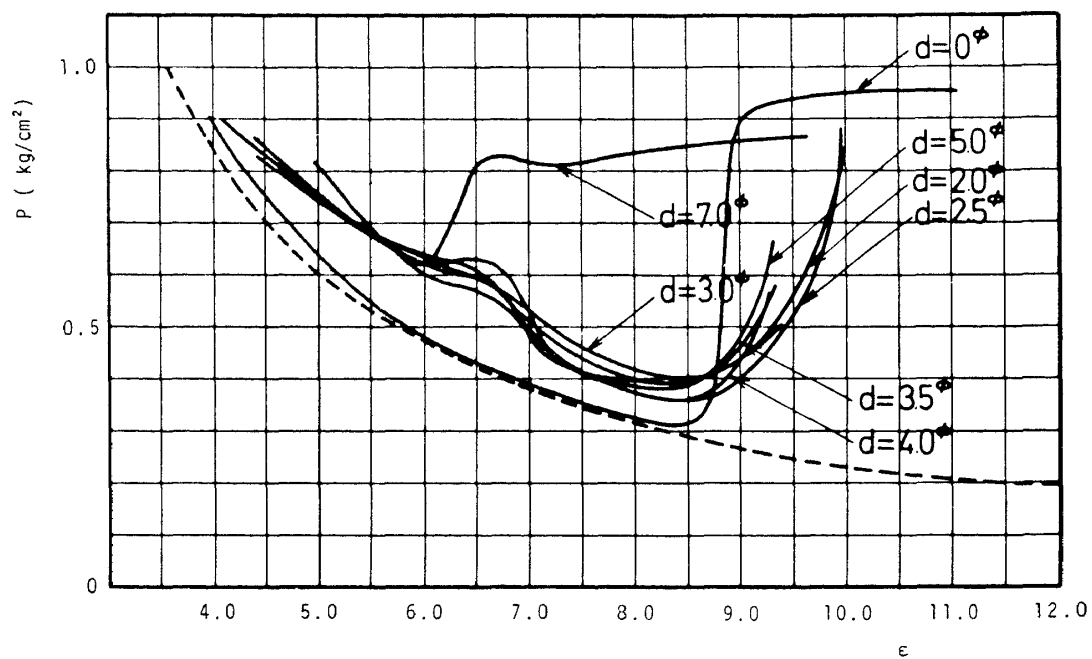
Fig.28 Pressure distribution measurement on the nozzle wall with hole at ε = 6.0
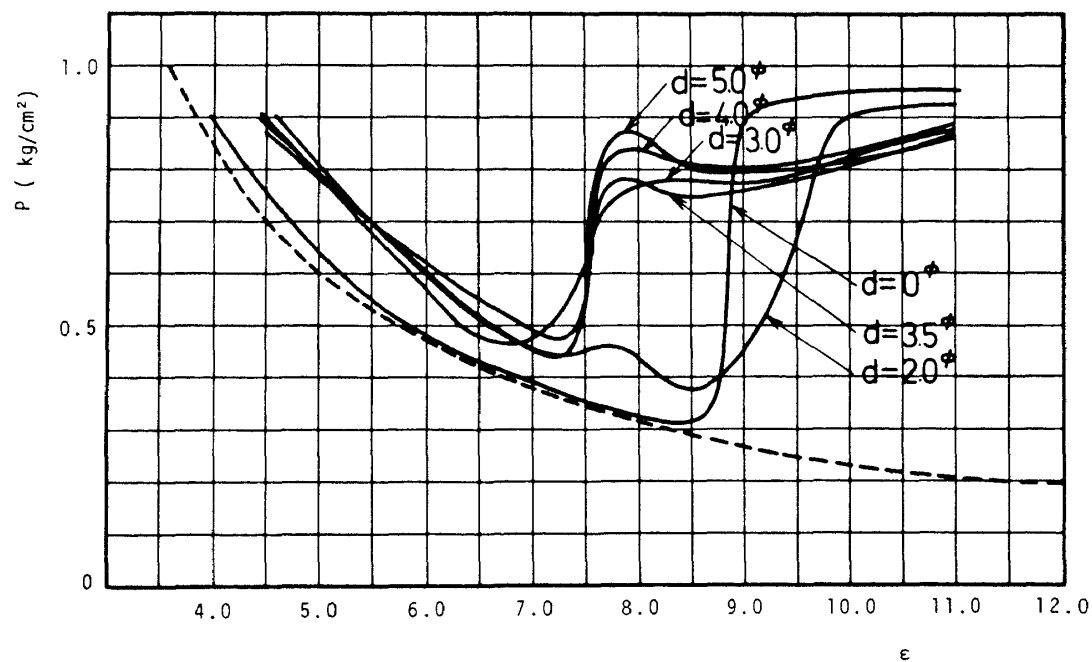
Fig.29 Pressure distribution measurement on the nozzle wall with hole at ε = 7.4

analytical result C_f with hole at the position of pressure P_k

S : sum of hole area s (S = n·s)

X : experimental results

analytical result of C_f with no hole

experimental result of C_f with no hole

P_k (kg/cm^2)
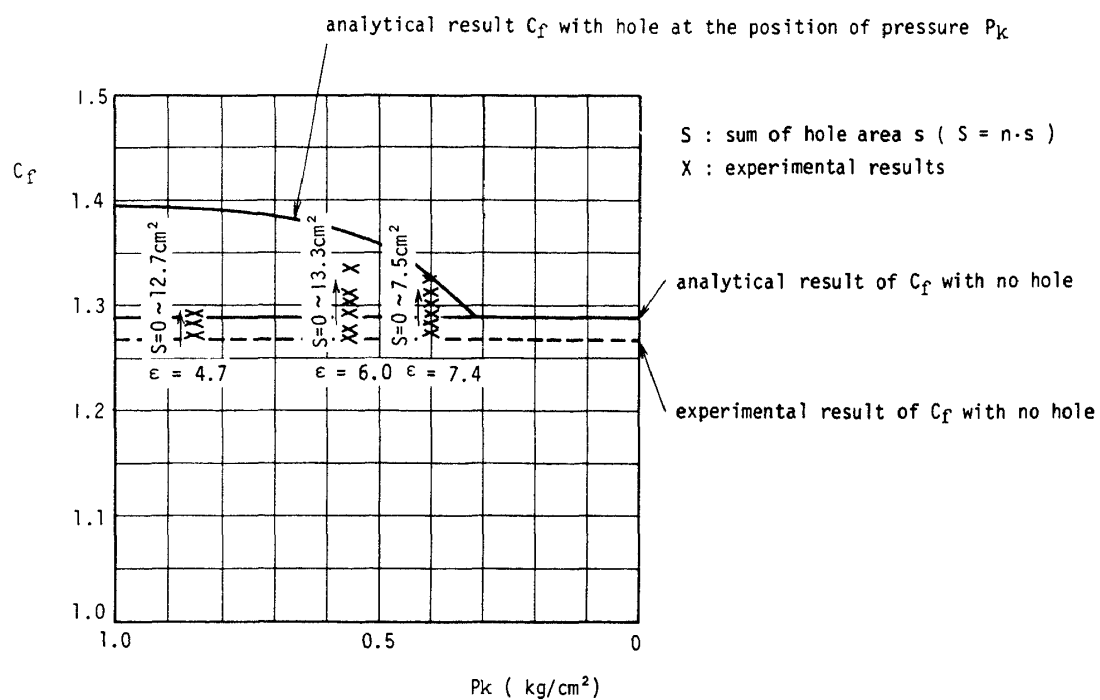
Fig.30 C_f measurement of nozzle with hole

(Pc = 19.8 kg/cm^2, P_A =1.0 kg/cm^2, ε = 12 , γ = 1.22)
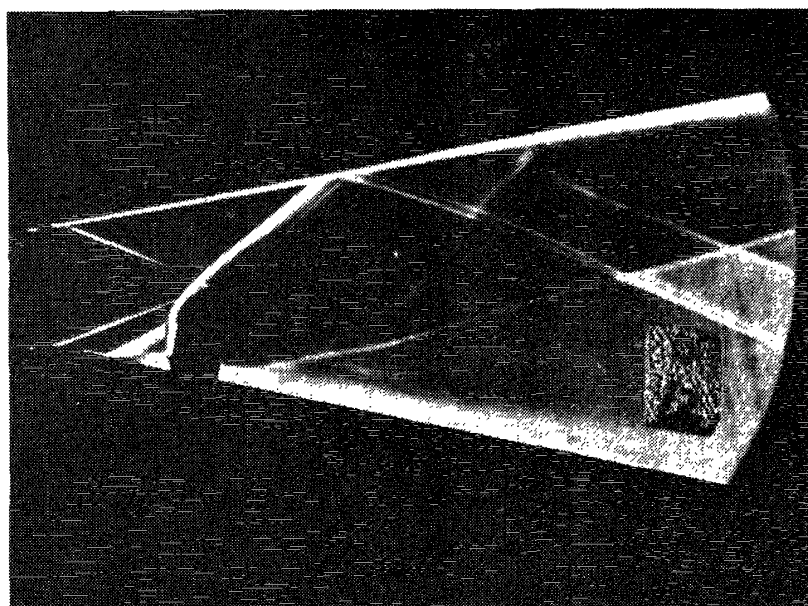
Fig.31   Shock wave induced by a cylindrical obstacle (h=12)
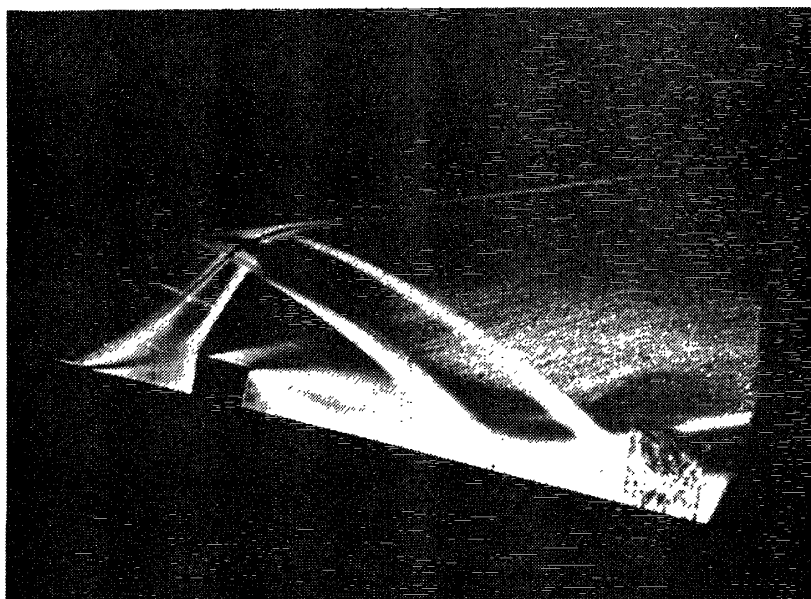
Fig.32   Shock wave induced by a two dimensional rectangular block obstacle (h=10)
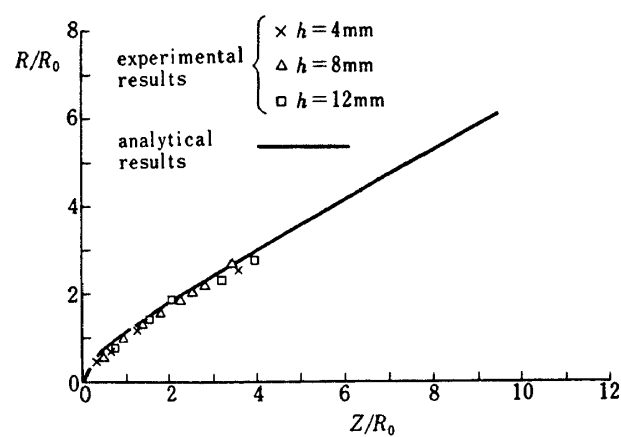
Fig.33 Normalized radius of the shock wave induced
by cylindrical type obstacles
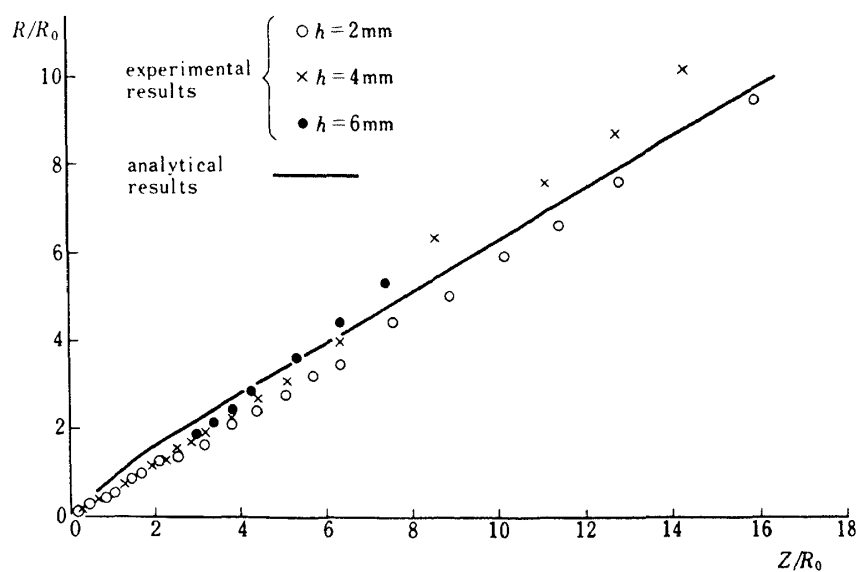
Fl .'4 'Normalized radius of the .hock wave induced by rectangular blocks
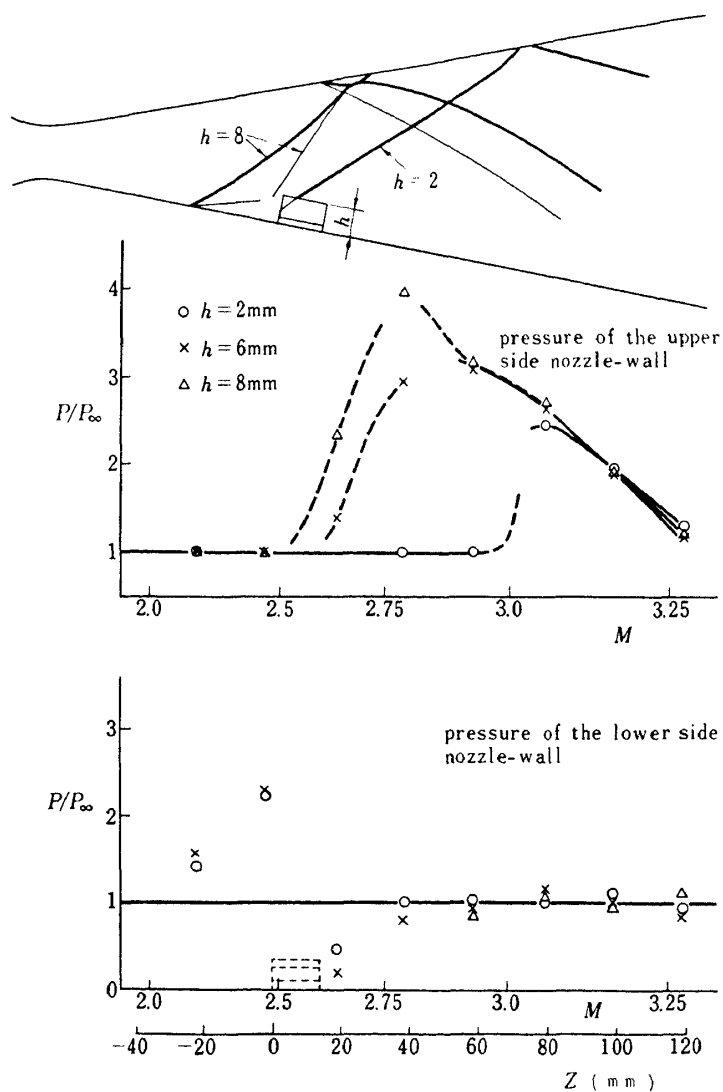
Fig.35 Pressure distribution
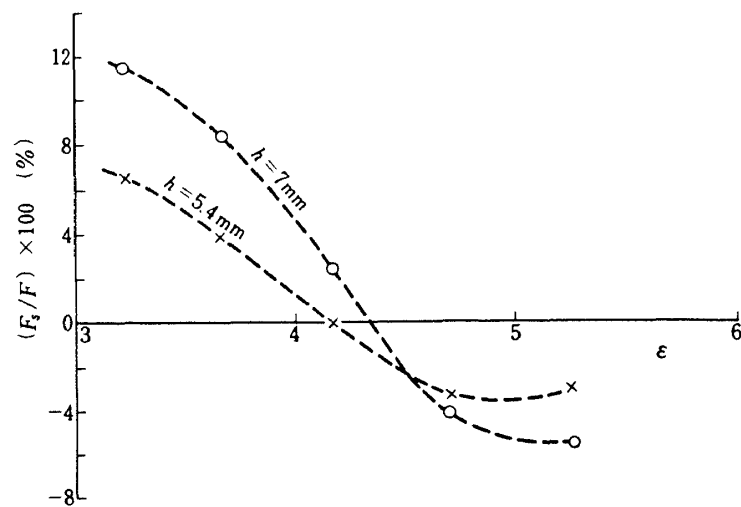
Fig.36 The experimental result of the side force
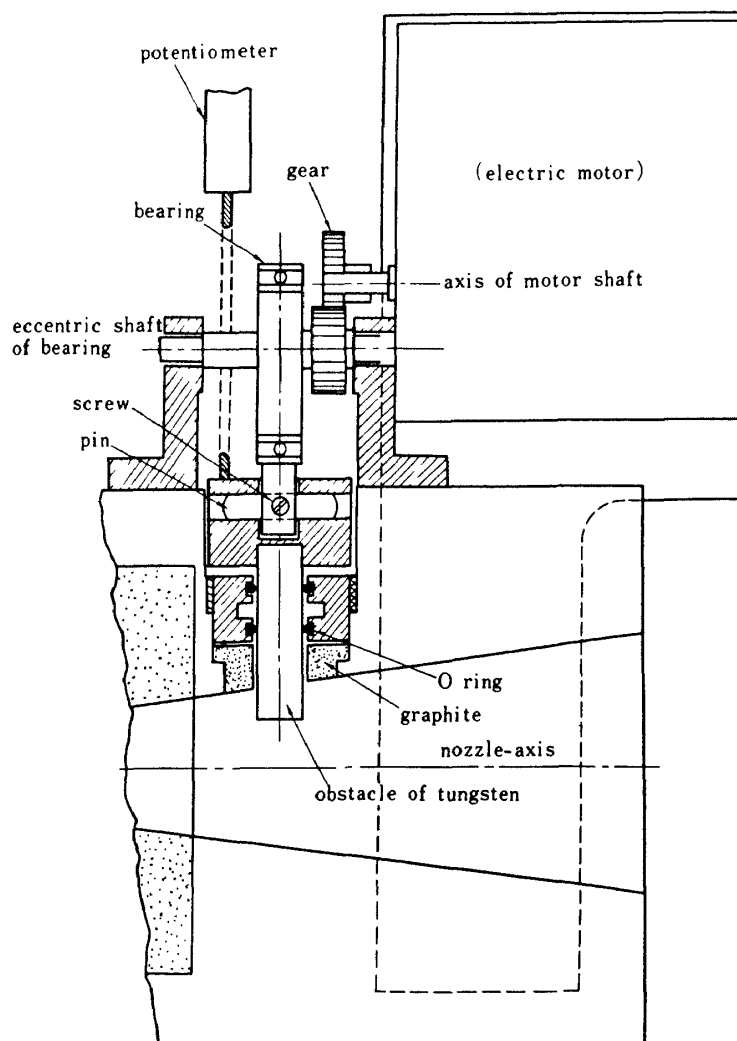
Fig.37 The nozzle with actuator of an obstacle
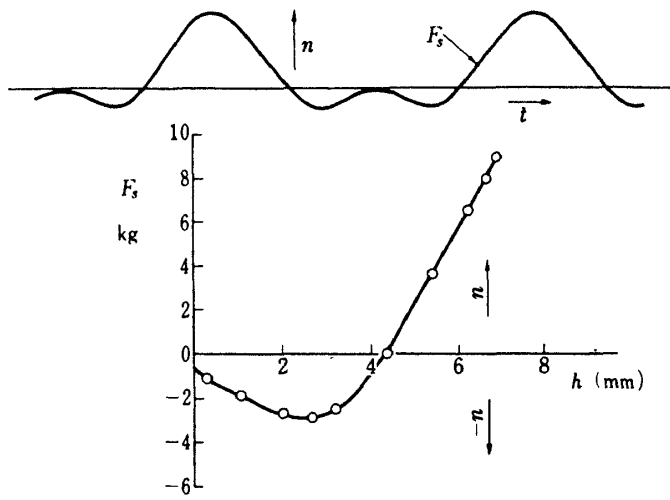
Fig.38   The side force $(\varepsilon = 3.7, \ f = 1.3 \text{cps})$
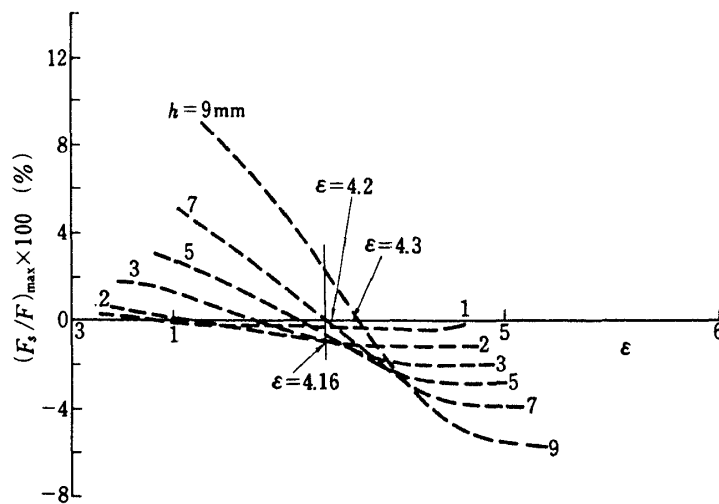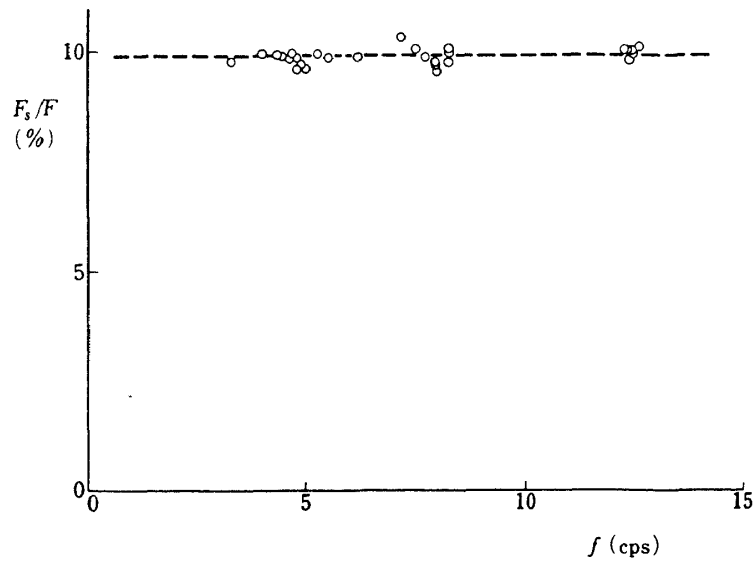

Fig.39   The dependence of side force on the parameter h

Fig.40 Frequency response of side force
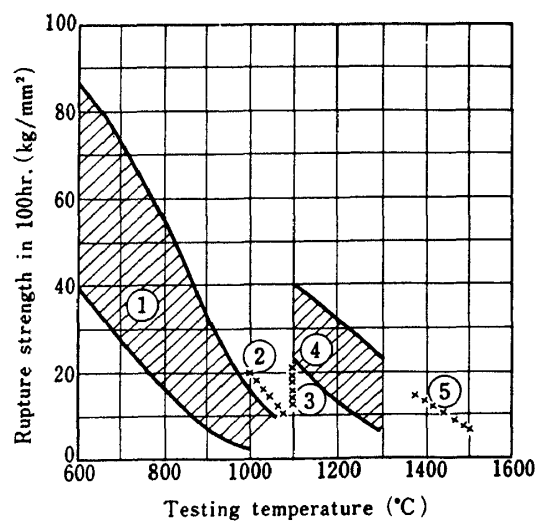
(1) Ni base refractory alloy, Co base refractory alloy.
(2) Cr base refractory alloy.
(3) Cb base refractory alloy.
(4) Mo base refractory alloy.
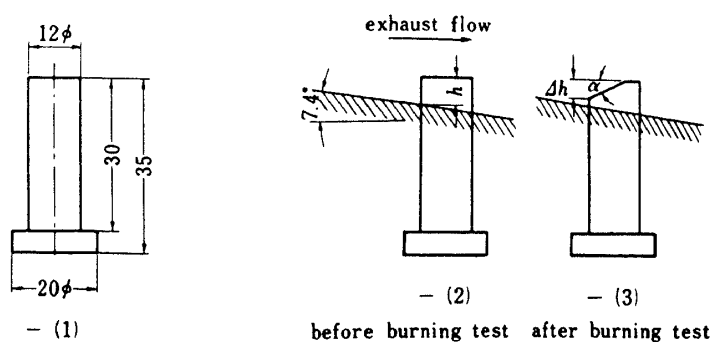(5) W   base refractory alloy.

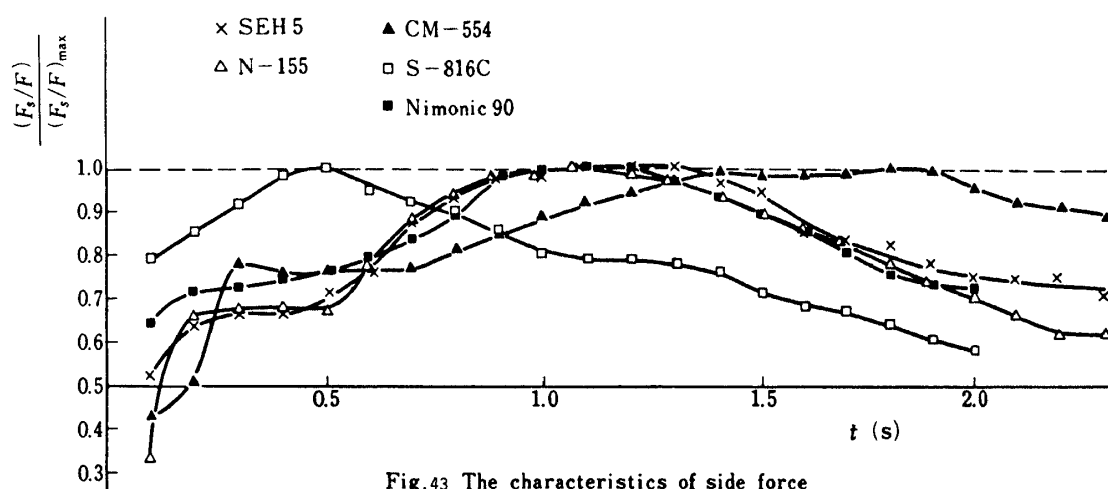Fig.41 Rupture strength of refractory alloys in 100 hr.

Fig.42 Obstacle

x SEH 5 ▲ CM−554
△ N−155 □ S−816C
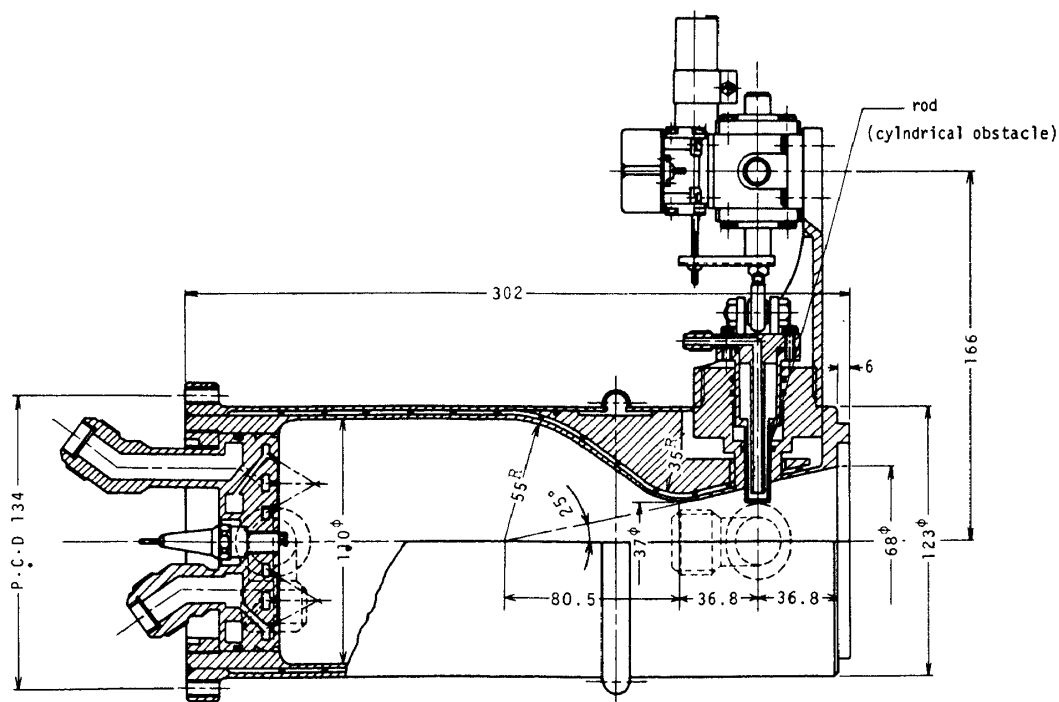■ Nimonic 90

Fig.43 The characteristics of side force

Fig.44-1 Liqud propellant rocket engine with rod hight control system

Fig.44-2 Rod hight control apparatus
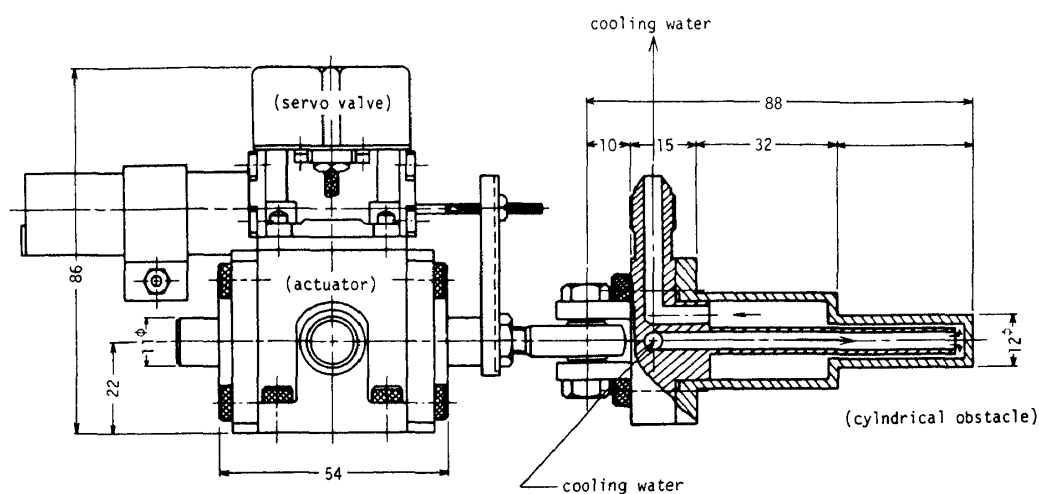
Table 3 Chemical composition of the refractory materials (%)

	Material	Fe	Cr	Ni	Co	Mo	W	Cd	C	Ti	Al	N	Melting point (C)	Specific gravity
Fe base	SUS 27	Bal	18	8	—	—	—	—	0.06	—	—	—	650 ~ 800	7.89
Fe base	S25C	Bal	-	--	—	—	—	—	0 25	—	—	—	650 ~ 800	7.85
Fe base	SEH5	Bal	25	20	—	—	—	—	0.2	—	—	—	1396 ~ 1404	7.86
Fe base	N-155	Bal	20	20	20	3	2.5	1	0.12	—	—	0.12	1274 ~ 1357	8.21
Cr base	CM-554	25	Bal	—	—	15	—	—	—	2	—	—	1580 ~ 1648	7.85
Co base	S-816C	3	20	20	Bal	4	4	4	0.4	—	—	—	1307 ~ 1343	8.55
Ni base	Nimonic 90	—	20	Bal	18	--	--	—	—	2	1.5	—	1384 ~ 1400	8.22
C base	graphite G-113	—	—	—	—	—	-	—	Bal	—	—	—	3500	2.25
W base	tungsten	—	—	—	—	—	99	—	—	—	—	—	3410	18.9

Table 4 Experimental result of refractory materials

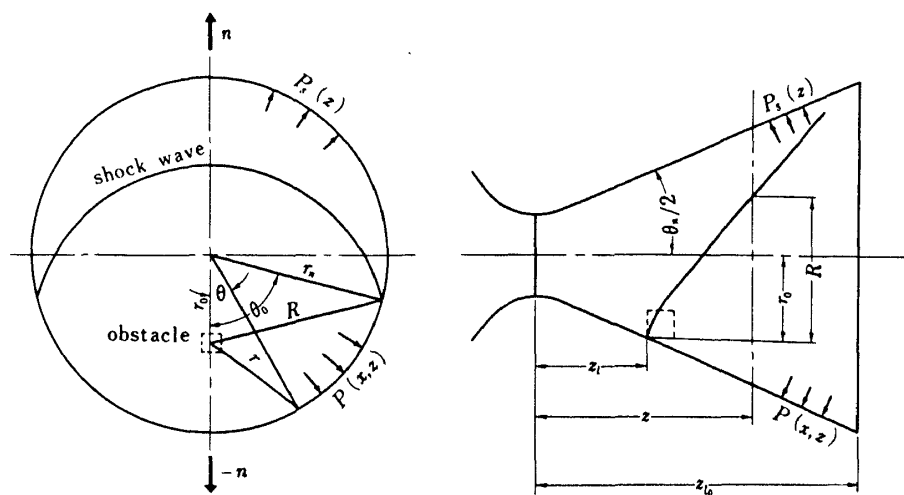| Material	h (mm)	Δh (mm)	ΔV (cm³)
SUS	4.6	4.1	
S25C	5.7	5.4	0.270
SEH5	5.4	5.0	0.240
N-155	5.4	5.0	0.242
CM-554	5.3	4.5	0.179
S-816C	5.4	4.9	0.323
Nimonic 90	5.4	4.7	0.238
graphite G-113	5.4	broken	broken
tungsten	5.4	0	0

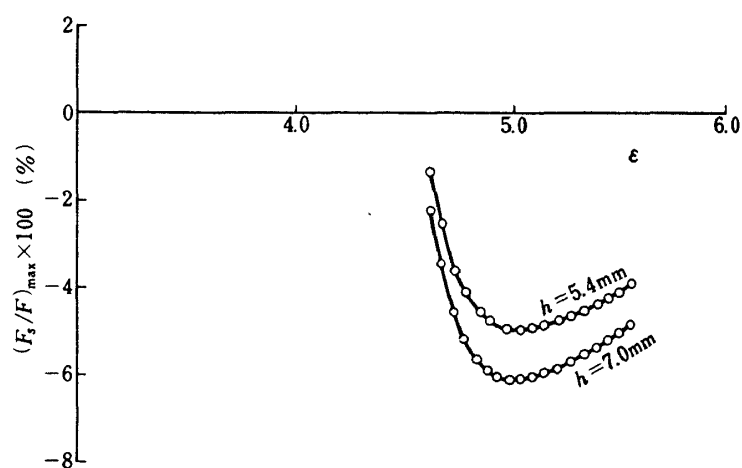Fig.45 The cross section of the nozzle and the pressure $p(x,z)$, $p_s(z)$
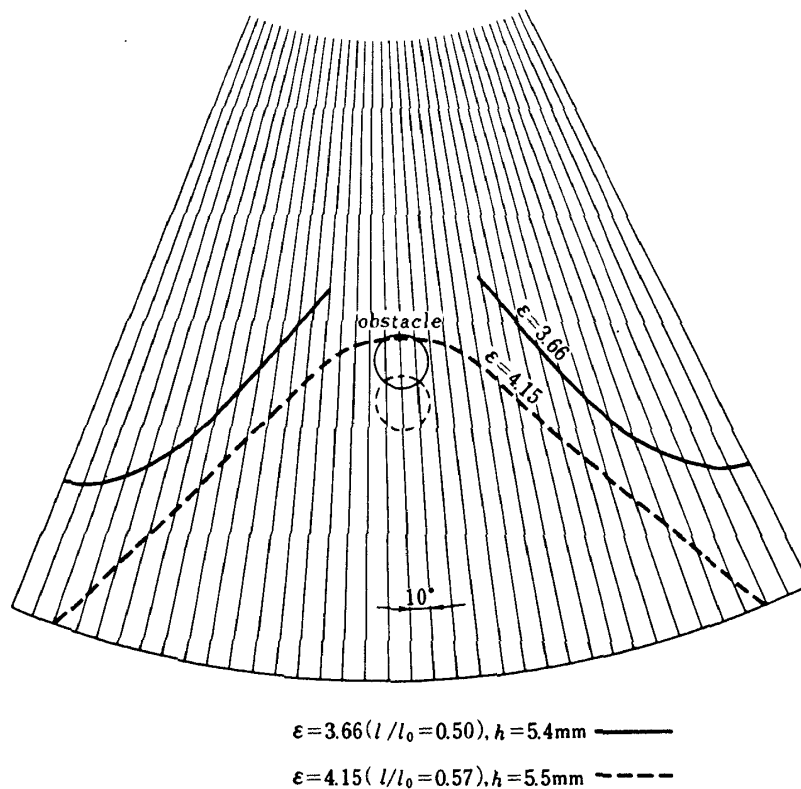

Fig.46 Analytical results of the side force

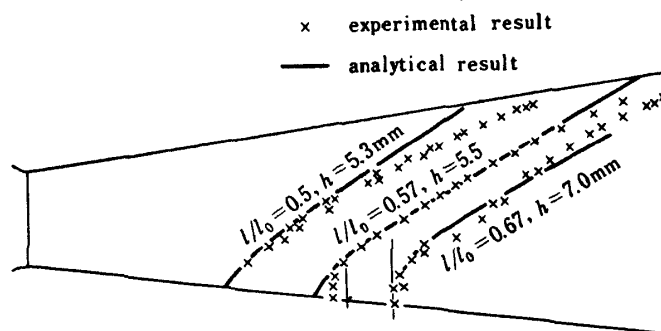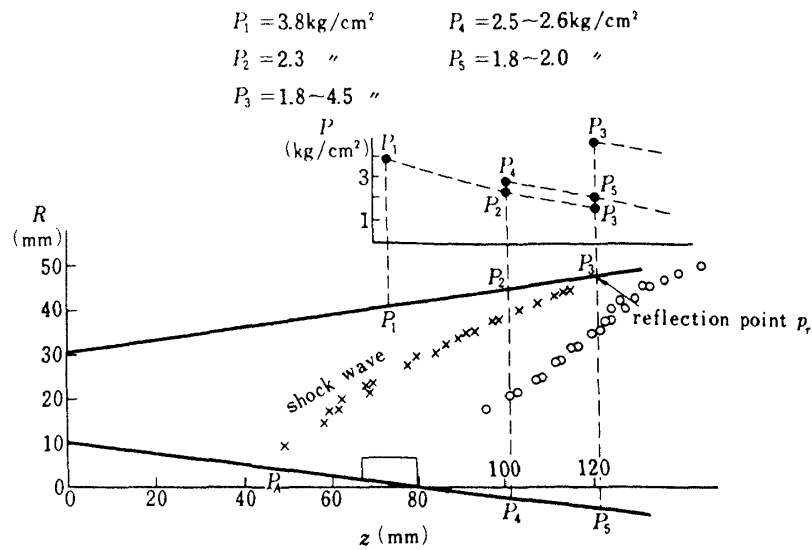$\varepsilon = 3.66(l/l_0 = 0.50)$, $h = 5.4$mm ────

$\varepsilon = 4.15(l/l_0 = 0.57)$, $h = 5.5$mm ── ── ──

Fig.47   The mark of the shock wave on the nozzle-wall

×   experimental result

───   analytical result

Fig.48   The radius R of the shock front in the nozzle

$P_1 = 3.8 \text{kg/cm}^2$ $P_4 = 2.5 \sim 2.6 \text{kg/cm}^2$

$P_2 = 2.3$ $''$ $P_5 = 1.8 \sim 2.0$ $''$

$P_3 = 1.8 \sim 4.5$ $''$

Fig.49 The pressure distribution p_i $(i = 1, 2, \cdots\cdots, 5)$

$\gamma = 1.25$
$h = 5.4 \text{mm}$
$\varepsilon = 2.8$ (———)
$\varepsilon = 3.5$ (————)

ΔF_s at the position z of nozzle-axis, which is the integration of the pressure along to the circular line on the cross section of the nozzle-wall

pressure distribution on the cross section A, B, C, of the nozzle-wall
$(\varepsilon = 3.5)$

Fig.50 The pressure distribution on the cross section of the nozzle-wall and its integration ΔF_s

Pritend in Japan